Multichannel singular spectrum analysis of InSAR datasets: data-adaptive interpolation and decomposition of Sentinel-1 time series at Pacaya Volcano, Guatemala

D. Walwer[1], J. Gonzalez-Santana[1], C. Wauthier[1,2], E. Calais[3,4]& M. Ghil[3,5,6]

[1]Department of Geosciences, The Pennsylvania State University, University Park, PA, USA
[2]Institute for Computational and Data Sciences, The Pennsylvania State University, University Park, PA, USA
[3]Département de Géosciences, École normale supérieure, Université PSL; Paris, France
[4]Université Côte d'Azur, Institut de Recherche pour le Développement, CNRS, Observatoire de la Côte d'Azur, Géoazur; Valbonne, France.
[5]Department of Atmospheric & Oceanic Sciences, University of California at Los Angeles, Los Angeles, CA, USA
[6]Department of Mathematics, Imperial College London, London, UK

Key Points:

- M-SSA is applied for the first time to analyze InSAR time series in a nonparametric, data-adaptive way
- The M-SSA gap-filling algorithm is used to produce at first evenly sampled InSAR time series
- Next, M-SSA decomposes InSAR data at Pacaya volcano into spatio-temporal modes capturing seasonal oscillations and a nonlinear trend

Corresponding author: Damian Walwer, damianwalwer@gmail.com

Abstract

This paper presents the first application of multichannel singular spectrum analysis (M-SSA) to radar satellite geodesy. We apply M-SSA to Sentinel-1 Interferometric Synthetic Aperture Radar (InSAR) time series processed for Pacaya Volcano in Guatemala in two steps. First, we produce, in an iterative and data-adaptive way, estimates of missing data points to obtain evenly sampled time series. The resulting time series are then decomposed with M-SSA into long-periodic nonlinear trends and oscillatory modes providing a sparse representation of the signals present in the data. The M-SSA approach presented herein is designed to deal with very large datasets such as collections of InSAR time series. Combining M-SSA with power spectrum analysis show that the dominant frequencies of the main oscillatory modes correspond to 1, 1.5, 2, 3, 5.8 and 6.8 cycle per years. These frequencies are consistent with the seasonal variability of the regional hydrological system, as determined from correlograms of rainfall time series and M-SSA modes extracted from time series of regional gravity anomalies using Gravity Recovery and Climate Experiment (GRACE) data, Global Navigation Satellite Systems (GNSS) time series recorded in Guatemala City, and phase delay maps derived from a global weather model. While some of the seasonal oscillations correlate well with topography, others show significant spatial asymmetries. The extracted nonlinear trends show large amplitudes around the summit and within the area covered by the 2014 lava flows and, to a lesser extent, the 2010 lava flows. This nonlinear trend correlates with interannual variability of the regional water cycle.

Plain Language Summary

InSAR time series capture sometimes surface displacements caused by volcanic, seismo-tectonic and hydrological processes. As such, these series can help monitor and understand interesting geophysical phenomena. These geophysical signals might, however, be blurred by measurement noise. Here we apply multichannel singular spectrum analysis (M-SSA) to analyze InSAR time series recorded at Pacaya volcano in Guatemala. M-SSA is a methodology that helps filter out the noise and decompose a set of time series into components that correspond to different geophysical phenomena. M-SSA is data driven and does not require a priori information on the signals one wants to extract from the dataset at hand. The methodology relies on the spatio-temporal correlations of geophysical fields from which a set of empirical functions is extracted and used to represent the information contained in the time series being analyzed simultaneously. At Pacaya, M-SSA decomposes the InSAR time series into components capturing seasonal oscillations, as well as a trend of variable slope that correlates with multiannual fluctuations of the regional hydrological cycle.

1 Introduction

Interferometric Synthetic Aperture Radar (InSAR) uses the difference in phase between radar images acquired at different times from satellite or aircraft platforms to produce surface displacements over a given area (Massonnet & Feigl, 1998; Simons & Rosen, 2007). InSAR provides quasi-continuous spatial coverage compared to the discrete measurements provided by Global Navigation Satellite Systems (GNSS). InSAR reveals deformation patterns that contain information about the source and mechanism of seismic events, volcanic unrest, as well as other natural phenomena such as landslides or ground water variation (Massonnet et al., 1995; Jolivet et al., 2013; Béjar-Pizarro et al., 2017). By combining multiple SAR scenes covering the same geographic location over time, we can produce InSAR time series of surface displacements that allow us to also study the kinematics and dynamics of the underlying natural phenomena (e.g., Lundgren et al., 2001; Hooper et al., 2012; Jolivet et al., 2013; Biggs et al., 2010; Pinel et al., 2014).

However, the objective extraction of time-dependent volcanic or seismo-tectonic geophysical signals from InSAR time series remains a challenge. These signals are mixed with colored noise from various sources, including for example, atmospheric delays, referencing

issues, decorrelation or processing errors (Jolivet et al., 2011, 2014; Stephens et al., 2020). InSAR can also contain harmonic signals, usually seasonal in period, that may be caused by variations in hydrological and atmospheric loads, pore pressure fluctuations in aquifers, or stress changes induced by seasonal temperature variations within the ground (Prawirodirdjo et al., 2006; Chanard et al., 2018; Larochelle et al., 2021). Being able to discriminate seasonal deformation patterns from signals of seismo-tectonic or volcanic origin is critical for a proper interpretation of geodetic time series (e.g., Chanard et al., 2020; Li et al., 2023).

In addition, seasonal deformations, on their own, do contain geophysical information about the solid Earth. Spatial variations of their amplitude and phase are a function of the subsurface structure as well as of crustal mechanical properties, hence providing a way to probe these geophysical features (Chanard et al., 2018; Larochelle et al., 2018). Seasonal deformation patterns in geodetic time series also offer the opportunity to study the relationships between seismo-tectonic or volcanic events and environmental forcing mechanisms (e.g., Bettinelli et al., 2008; Craig et al., 2017; Lundgren et al., 2022).

The methods used to unravel the different types of signals from noise in both InSAR and GNSS time series have been the subject of recent studies. These methods often rely on a priori knowledge or assumptions about the signals of interest but may also be data adaptive. Adjusting analytical functions to the data through deterministic or probabilistic inversion schemes exemplifies the former approach while principal component analysis (PCA) is a classical example of the latter (e.g., Preisendorfer, 1988; Riel et al., 2014; Ebmeier, 2016; Dalaison & Jolivet, 2020).

Machine and deep learning offer promising perspectives for the automatic detection and classification of deformation patterns in large datasets (Anantrasirichai et al., 2018). Both require "training" the algorithm, i.e., feeding it with a large amount of data in order for it to "learn" how to detect signals of interest (e.g., Sun et al., 2020; Rouet-Leduc et al., 2021). The datasets used for the training process are often synthetic because of the large amounts required for the learning algorithms to be effective, a quantity that geodetic measurements of natural systems alone cannot provide (Rouet-Leduc et al., 2021). These synthetics are built using source and noise models that constitute a priori information about the deformation patterns one wants to extract from InSAR time series, as well as the temporal and spatial structure of the noise. For example Rouet-Leduc et al. (2021) produced synthetics using either Okada or Mogi models with parameter ranges representing the range of possible depths and geometries of the expected deformation sources (Kiyoo, 1958; Okada, 1985). While justified in some cases, such a procedure may limit the identification and extraction of signals to the ones that possess expected characteristics.

Independent component analysis (ICA) algorithms also received significant attention in recent studies of ground deformation (Ebmeier, 2016; Gualandi et al., 2016, 2017; Larochelle et al., 2018; Cohen-Waeber et al., 2018; Gaddes et al., 2019). Similar to PCA, ICA is data adaptive and decomposes geodetic time series into the components that provide a sparse representation of the information contained within a dataset. While PCA produces components that are spatially uncorrelated, ICA assumes that the time series being analyzed are linear combinations of components that are statistically independent, either spatially or temporally (Ebmeier, 2016). Although ICA can provide sparse representations of time series, it is always useful to consider alternative criteria for the data-adaptive decomposition of time series into their modes of spatio-temporal variability. For example, time series that are combinations of oscillations with different periods and phases, such as the seasonal deformation patterns present in many geodetic datasets, may be better represented by temporally uncorrelated components rather than by temporally independent components (Vautard & Ghil, 1989; Ghil et al., 2002; Walwer et al., 2016; Prevost et al., 2019). Furthermore, the components derived from ICA are ambiguous and cannot be sorted according to the percentage of variance they capture. Hence, ICA is sometimes used in combination with PCA

in order to obtain components that are ranked by order of importance (Hyvärinen & Oja, 2000; Cohen-Waeber et al., 2018).

Here, we apply a generalization of PCA, namely M-SSA, to analyze and decompose InSAR time series covering Pacaya Volcano in Guatemala and show that it provides an interesting alternative to InSAR analysis based on PCA, ICA, or machine learning. While in common geophysical terminology PCA refers to a nonparametric analysis that exploits solely spatial correlations between time series, M-SSA simultaneously uses temporal and spatial correlations. It has extensively been used to analyze time series in meteorology, oceanography, and climate sciences in general, especially thanks to its ability to extract and characterize oscillatory modes of variability — intraseasonal, interannual and interdecadal — such as the El Niño–Southern Oscillation (e.g., Ghil et al., 2002, and references therein). In geodesy, M-SSA has been successfully applied to analyze Global Navigation Satellite Systems (GNSS) and Gravity Recovery and Climate Experiment (GRACE) time series and extract both long-term trends and seasonal oscillations, even in the presence of significant noise levels (Walwer et al., 2016; Craig et al., 2017; Prevost et al., 2019; Walwer et al., 2022).

In Secs. 2 and 3, we review the regional geological context of Pacaya Volcano and introduce the InSAR datasets used in this study. We then present in Sec. 4.1 the main steps of the M-SSA algorithm and provide a more detail account of the M-SSA methodology compare to previous M-SSA applications in geodesy. M-SSA is then applied in two different ways. In Sec. 4.2, we first use it to produce evenly-sampled InSAR time series in an iterative and data-adaptive way. Then, in Sec. 4.3, we introduce an approach to apply M-SSA algorithm on very large datasets and apply it to the resulting, evenly-sampled, time series in order to decompose the dataset into its main components of spatio-temporal variability. The main results are presented in Sec. 5 followed by the discussion of both oscillatory modes and the nonlinear trend in Sec. 6 and conclusions in Sec. 7.

2 Background: Pacaya Volcano, Guatemala

Pacaya is an active volcano in Guatemala. It has exhibited frequent volcanic unrest in recent years, including summit activity and major flank eruptions in 2010 and 2014 (Gonzalez-Santana & Wauthier, 2021); see Figure 1. Pacaya's southwestern flank is also prone to slope instabilities (Schaefer et al., 2019), with broad flank motion likely modulated by magmatism, specifically edifice-wide dike intrusions and eruptions from aligned vents (Gonzalez-Santana & Wauthier, 2021; Gonzalez-Santana et al., 2022a). Pacaya exhibited its largest recorded flank motion of roughly 3 m during the May 2010 eruptive episode (Schaefer et al., 2015). Smaller amplitude flank motion was also noticed during another large eruption in January–March 2014 (Wnuk & Wauthier, 2017). Both scenarios were followed by years of slow creep of less than 2 cm/yr during the relative volcanic quiescence of 2010–2014 and 2015–2018 (Gonzalez-Santana & Wauthier, 2021; Gonzalez-Santana et al., 2022a).

Ground deformation at Pacaya results in part from time-dependent magma storage and transport processes in the underlying magma plumbing system, including magma transport through dike emplacements and shallow or deep reservoir pressure fluctuations (Wnuk & Wauthier, 2017). Other sources of ground deformation revealed by InSAR are lava flow compaction and creep on the southwest flank (Gonzalez-Santana & Wauthier, 2021). However, a detailed characterization of magmatic and faulting deformation signals at Pacaya is challenging due to (a) the presence of vegetation and steep slopes, which reduce the coherence of InSAR products; and (b) the large seasonal change in tropospheric water vapor content, which introduces fluctuations in InSAR time series that are not related to surface deformation (Ebmeier et al., 2013; Gonzalez-Santana & Wauthier, 2021).

3 Data

Our main data source is provided by InSAR datasets from the European Space Agency's Sentinel-1 mission, which comprises two polar-orbiting satellites that acquire imagery regardless of cloudiness and weather: Sentinel 1A was launched in 2014 and is still operational,while Sentinel 1B was launched in 2016 but failed in December 2021. We also use complementary datasets of GNSS time series recorded in Guatemala City, at about 30 km from Pacaya summit; equivalent water height time series from the GRACE gravity field mission; daily rainfall time series; and zenith tropospheric delay maps from the Generic Atmospheric Correction Online Service for InSAR (GACOS).

3.1 Sentinel-1 InSAR datasets

Here, we focus on an InSAR time series covering Pacaya Volcano processed from Sentinel-1 SAR scenes acquired between 2015 and 2021 (Gonzalez-Santana et al., 2022a). The dataset is publicly available through ScholarSphere (https://scholarsphere.psu.edu/; `doi.org/10.26207/606g-5s27`; Walwer et al. (2023)) and was processed using the Multidimensional Small BAseline Subset (MSBAS) methodology that combines ascending and descending acquisitions (displayed in Figure S1 of the supplementary materials) to produce maps of vertical and East-West displacements. Examples of Sentinel-1 displacement maps and time series produced this way for Pacaya are displayed in Figure 2. The main characteristics of the dataset are summarized in Table 1 and further information on vertical and East–West displacement processing are provided in Gonzalez-Santana and Wauthier (2021) and reviewed in supplementary materials Text S1.

The Sentinel-1 dataset used herein possesses several features that highlight the benefits of the M-SSA methodology for InSAR time series analysis. As is common for InSAR time series, the sampling time interval is not constant. This sampling variability is due to the irregular nature of SAR scene acquisitions. Here, for example, the time interval between 2015 and 2017 is undersampled compared to the interval between 2017 and 2021, as seen in Figure 2b. To overcome this limitation, we first present an approach to produce evenly sampled time series directly based on the M-SSA algorithm (Kondrashov et al., 2005; Kondrashov & Ghil, 2006; Kondrashov et al., 2010).

The dataset we use was originally collected to explore the persistence of flank creep signals at Pacaya beyond the 2014 transient instability event; in addition, it revealed annual cyclicities that appeared to correspond to pronounced seasonality in Guatemala's atmospheric humidity. This feature made it an ideal dataset to apply M-SSA in order to to unravel the seasonal components from other potential geophysical signals and to study their characteristics. The vertical displacement at pixel $(-90.6120, 14.3684)$ readily displays seasonal oscillations with a frequency content that appears to correspond to harmonics of annual oscillations; see Figure 2b. The amplitude and phase modulations of these seasonal oscillations would be difficult to capture by simply adjusting harmonic functions of annual or subannual period to the time series (e.g., Walwer et al., 2016). Whether the horizontal component captures seasonal patterns of deformation is not as clear as for the vertical one; see again Figure 2b.

The Sentinel-1 InSAR time series also present pixels with nonlinear trends — i.e., long-term trends with a varying slope — whose amplitudes depend on pixel location. Such a nonlinear trend is readily visible in Figure 2b for the time series corresponding to the vertical displacement at pixel $(-90.6082, 14.3546)$.

The cause of nonlinear trends in time series may vary from one dataset to another (Ghil et al., 2002, and references therein). At volcanoes, it may reflect the dynamics of magma movement occurring in the underlying crust (e.g., Walwer et al., 2016). In other cases, it reflects the multiannual variability of the regional hydrological system (Larochelle et al., 2021). Here, we exploit M-SSA's ability to extract such a long-term temporal pattern to

provide information on its spatio-temporal characteristics, as well as to explore its possible origin.

Successful time series analysis involves unravelling these nonlinear trends from the seasonal oscillations, in order to isolate signals relevant to the study of magmatic, faulting, or hydrological sources of ground deformation. As explained in the following section, M-SSA offers the opportunity to do so without having to arbitrarily choose analytical functions that best describe the shape of those trends (e.g., Ghil et al., 2002; Alessio, 2016; Walwer et al., 2016; Prevost et al., 2019).

3.2 Complementary datasets

In order to test and, if possible, validate the reliability of the M-SSA findings for InSAR time series recorded at Pacaya, we gathered additional datasets that are relevant in various ways for the spatio-temporal patterns of the regional hydrological regime. If part of the extracted spatio-temporal patterns with M-SSA is caused by regional hydrological phenomenon causing deformation or introducing atmospheric artefacts such as atmospheric phase delay, i.e., in fluctuations caused by changes in tropospheric water content that affect radio wave propagation between satellite and the ground, they are expected to share similarities in frequency contents with patterns present in other datasets and related by the same regional environmental processes.

GNSS time series recorded in Guatemala City. We obtained the East, North and vertical components of the time series recorded at GNSS station GUAT in Guatemala City from the Nevada Geodetic Laboratory (geodesy.unr.edu); see Figure 3a (Blewitt et al., 2018). Although this GPS station is not located on Pacaya volcano, but ∼30 km from it, its time series covers the exact same time interval as the Sentinel-1 InSAR dataset recorded at Pacaya. We use it to determine whether it shares common spectral characteristics with the InSAR time series resulting from variability in the regional hydrology.

Equivalent water height time series from GRACE. GRACE time series capture temporal variations of the Earth's gravity field. Over land, one of the main contributions to the Earth gravity field variations in GRACE solutions corresponds to the water mass redistribution. Here, we use GRACE time series expressed in millimeters of equivalent-water height (EWH) from the fifth release (RL5) of CNES's Groupe de Recherche de Géodésie Spatiale (GRGS) solutions with a 10-day resolution as an estimate of the surface and groundwater mass variation in the Guatemala region; see Figure 3b. These variations can induce seasonal and interannual deformation signals possibly captured by both InSAR data and GPS data covering Guatemala (Silverii et al., 2016; Larochelle et al., 2021).

Daily rainfall time series. In addition, we compiled a rainfall time series from the joint NASA–Japan Aerospace Exploration Agency (JAXA) Tropical Rainfall Measurement Mission and Global Precipitation Measurement mission data at `https://doi.org/10.5067/TRMM/TMPA/3H/7` to compare the variability extracted from InSAR with the timing of wet and dry seasons at Pacaya. The rainfall time series in Figure 3d corresponds to the daily rainfall precipitation expressed in millimeter during the time interval 2015–2021.

Zenith tropospheric delay maps from GACOS. Finally, we downloaded zenith tropospheric delay (ZTD) maps from the Generic Atmospheric Correction Online Service for InSAR (GACOS); see `http://www.gacos.net/` (Yu et al., 2017; Yu, Li, Penna, & Crippa, 2018; Yu, Li, & Penna, 2018). Tropospheric delay maps correspond to estimates of the spatio-temporal change in meters within the InSAR data that could result from variability in tropospheric water vapor over Pacaya rather than actual deformation of the Earth. We downloaded ZTD maps for every other day during the time interval captured by the Sentinel-1 scenes of Pacaya; see Figure 3c. Contrary to the complementary data listed so far, the ZTD dataset consists in maps and can provide additional information on spatial

patterns that may be present within the InSAR scenes analyzed herein. As such, the spatial structures extracted from the Sentinel-1 dataset with M-SSA can be compared to the ones present in the ZTD maps.

4 Methods

M-SSA codes as well as a demo reproducing results presented herein are publicly available through ScholarSphere; see https://scholarsphere.psu.edu/; `doi.org/10.26207/606g-5s27`; and Walwer et al. (2023).

4.1 Multichannel Singular Spectrum Analysis (M-SSA)

Before describing the specifics of applying M-SSA to InSAR time series, we first present the steps that constitute the core of the M-SSA algorithm. These steps rely on a few basic algebraic operations and confer to M-SSA a fairly straightforward, transparent, and reproducible character. Like PCA, M-SSA extracts a base of empirical orthogonal functions (EOFs) and principal components (PCs) from the eigenvalue decomposition of a covariance matrix constructed from a set of time series. While PCA exploits solely spatial correlations, M-SSA simultaneously makes use of spatial and temporal correlations between time series (Ghil et al., 2002; Alessio, 2016, Ch. 12).

Formally, M-SSA decomposes a set of D time series of N data points with a constant sampling interval τ_s into their modes of spatio-temporal variability. Let $x_\ell(t)$ be the time series one wishes to decompose, with $\ell = 1, \dots, D$ and $t = 1, \dots, N$.

The modes one is interested in are derived from the eigendecomposition of either the covariance matrix

$$\mathbf{C}^{(V)} = \frac{1}{(N')} \mathbf{X}^\mathrm{t} \, \mathbf{X} \tag{1}$$

or the complementary covariance matrix:

$$\mathbf{C}^{(P)} = \frac{1}{(DM)} \mathbf{X} \mathbf{X}^\mathrm{t}. \tag{2}$$

Here $(\cdot)^\mathbf{t}$ stands for the transpose and both $\mathbf{C}^{(V)}$ and $\mathbf{C}^{(P)}$ are computed from the ensemble of M lagged copies of the D time series composing the dataset and forming the columns of the matrix $\mathbf{X} = (\mathbf{X}_1, ..., \mathbf{X}_\ell, ..., \mathbf{X}_D)$, where

$$\mathbf{X}_\ell = \begin{pmatrix} x_\ell(1) & x_\ell(2) & \cdots & x_\ell(M) \\ x_\ell(2) & x_\ell(3) & \cdots & x_\ell(M+1) \\ \vdots & \vdots & \ddots & \vdots \\ x_\ell(N') & x_\ell(N'+1) & \cdots & x_\ell(N) \end{pmatrix} \tag{3}$$

and $N' = N - M + 1$. Each of the M time series in (3) is delayed with respect to the original one by a lag that ranges from τ_s to $M\tau_\mathrm{s}$. The $(DM)^2$ elements contained in $\mathbf{C}^{(P)}$ are therefore lag-covariances computed from all possible pairs of the MD series contained in the columns of $\mathbf{X}$. Alternatively, the $(N')^2$ elements contained in $\mathbf{C}^{(V)}$ are lag-covariances computed from all possible pairs of the N' series contained in the columns of $\mathbf{X}^\mathbf{t}$.

The eigendecompositions of the covariance matrices $\mathbf{C}^{(V)}$ and $\mathbf{C}^{(P)}$, respectively, are given by

$$\mathbf{C}^{(V)} \mathbf{V}_k = \lambda_k^V \mathbf{V}_k, \tag{4a}$$

$$\mathbf{C}^{(P)} \mathbf{P}_k = \lambda_k^P \mathbf{P}_k. \tag{4b}$$

These decompositions yield the real positive eigenvalues λ_k^V and λ_k^P, as well as the corresponding eigenvectors $\mathbf{V}_k$ and $\mathbf{P}_k$, with k ranging respectively from 1 to DM and from 1

to N'. Signals that are strongly correlated in space and time in a given dataset are captured as the modes with the largest eigenvalues. Typically, in analyzing experimental time series, one finds that a few eigenvalues $\{\lambda_k^{V,P} : k = 1, \ldots, K\}$, with $K \ll \min\{DM, N'\}$, are separated by a jump or, at least, by a break in the slope of the singular spectrum $\{(\lambda_k^{V,P})^{1/2} : k = 1, \ldots, N^*\}$, in decreasing order, from the much more numerous small eigenvalues lying in the interval $K < k \leq N^*$, where $N^* = N'$ or DM, accordingly. Naturally, one concentrates the study on the leading eigenvalues and eigenvectors.

The EOFs $\mathbf{E}_k$ are either just the $\mathbf{V}_k$ or they can be obtained as follows:

$$\mathbf{E}_k = \mathbf{V}_k = \frac{1}{\sqrt{\lambda_k (N)'}} \mathbf{X}^t \mathbf{P}_k. \tag{5}$$

Upon proper scaling, both covariance matrices provide the same EOFs associated with the nonzero eigenvalues (Allen & Robertson, 1996; Ghil et al., 2002). The EOFs are formed by D successive segments $\mathbf{E}_{\ell k}$ of length M; each of them is associated with a time series $x_\ell(t)$ forming the datasets one wants to analyze.

The PCs $\mathbf{A}_k$ are time series of length N' that represent the temporal modulation of the extracted modes. They are obtained by projecting the time series and their lagged copies contained in matrix $\mathbf{X}$ upon the EOFs:

$$\mathbf{A}_k = \mathbf{X}\mathbf{E}_k. \tag{6}$$

The part of variance captured by each PC is given by its corresponding eigenvalue. The few leading PCs, i.e., those associated with the largest eigenvalues, are sparse representations of the time-dependent patterns shared across the set of time series. These PCs are a convenient tool for visualizing the temporal shape of the modes extracted with M-SSA, and help identify which modes may correspond to magmatic, seismo-tectonic, hydrological or seasonal signals. Alternatively, the EOFs, PCs and singular spectrum can be obtained by computing the singular value decompositions of Eqs. (4b, 4a); see Broomhead and King (1986); Vautard and Ghil (1989); Allen and Robertson (1996) and Text S2 herein.

Once the modes that correspond presumably to the geophysical signals of interest are identified, one can reconstruct the corresponding signal by projecting the PCs onto the EOFs:

$$\mathbf{R}_k = \mathbf{A}_k \mathbf{E}_k^{\mathrm{t}}. \tag{7}$$

The columns in $\mathbf{R}_k$ contain data-adaptively filtered versions of the time series forming the columns of $\mathbf{X}$ and have length N'. The final step of M-SSA is to produce filtered versions of the time series $x_\ell(t)$ of length N forming the original dataset. To do so, one computes the reconstructed components (RCs) by channel-wise averaging along skew diagonals of $\mathbf{R}_k$:

$$r_{\ell k}(t) = \frac{1}{M_t} \sum_{j=L_t}^{U_t} A_k(t - j + 1) E_{\ell k}(j). \tag{8}$$

The normalization factor M_t and the summation bounds L_t and U_t are simply $(M_t, L_t, U_t) = (M, 1, M)$ for the central part of the time series ($M_t \leq t \leq N - M + 1$); for their values at either end, see Ghil and Vautard (1991), Ghil et al. (2002), and supplementary materials Text S3. Any subset $\mathcal{K}$ of EOFs and PCs can be selected to produce RCs associated with the relevant modes of variability $r_{\ell\mathcal{K}}(t) = \sum_{k\in\mathcal{K}} r_{\ell k}(t)$. In the InSAR geodesy context, the RCs are filtered versions of the time series associated with the pixels that compose the InSAR scenes. As such, they can be used to represent the spatial deformation patterns of the extracted modes.

The filtering done this way is data adaptive, since the EOFs and PCs are determined by the data, and the number of lags M determines, in this interpretation, the window width $M\tau_\mathrm{s}$ through which one is looking at the data. We will refer to M as the window width parameter or window width for short, since τ_s is fixed and no confusion is possible.

In the following sections, the M-SSA algorithm from Eqs. (1) or (2) to (8) is relied upon in two different ways. In section 4.2, we apply it to produce evenly sampled InSAR time series using the iterative M-SSA gap filling algorithm of D. Kondrashov and colleagues (Kondrashov et al., 2005; Kondrashov & Ghil, 2006; Kondrashov et al., 2010). This first step is necessary in order to then be able to apply M-SSA. In section 4.3, we then use M-SSA to decompose the resulting set of evenly sampled InSAR time series into their modes of spatio-temporal variability. This allows us to separate signals of geophysical interest from noise and to associate the former with specific geophysical processes in section 6.

4.2 M-SSA gap filling

M-SSA requires the computation of either one of the covariance matrices $\mathbf{C}^{(V)}$ or $\mathbf{C}^{(P)}$ obtained from M copies of a set of time series delayed by a constant time interval τ_s, as described in Section 4.1. InSAR time series, however, are often constructed from SAR scenes acquired with irregular time sampling. Here, we describe a gap filling approach that exploits M-SSA's ability to reconstruct filtered versions of time series, namely the RCs $r_{\ell k}(t)$ of equation (8). M-SSA gap filling benefits from one of M-SSA's main features: it is data adaptive and does not rely on a priori knowledge or assumptions about the spatio-temporal structure of the dataset (Kondrashov et al., 2010). Being able to produce evenly sampled InSAR time series is also useful for applying spectral analysis — as demonstrated below — or inversion schemes that require a constant sampling time interval.

Iterative M-SSA gap filling. The M-SSA gap filling algorithm iteratively produces estimates of the missing data. The algorithm starts with a user-assigned choice of constant sampling time τ_s. Here, we choose the largest sampling time interval that allows us to retain all original data points while adding the least possible new data points. For the Sentinel-1 time series used here, this choice corresponds to $\tau_\mathrm{s} = 2$ days.

The algorithm starts by removing the mean of each time series and normalizing it to unit variance. Missing values are initially set to zero in order to obtain a first estimate of the covariance matrix $\mathbf{C}$ using Eqs. (1) or (2), with $\mathbf{C}$ being the smaller one, in dimension, of $\mathbf{C}^{(V)}$ or $\mathbf{C}^{(P)}$, depending on $N' \gtrless DM$. To compute the elements of $\mathbf{C}$, it is necessary to chose a value for the window width parameter M; see section 4.1. Because we cannot determine a priori which value of M is the most appropriate for the purpose of estimating missing data points, we apply the gap filling algorithm using several values of M and evaluate the optimal value a posteriori, as described further below.

Once this initial $\mathbf{C}$ is produced, we compute the $r_{\ell 1}(t^*)$, where the t^* are the epochs of the missing data points, by using equation (8), and providing therewith initial estimates for the missing data points. We then carry out an inner-loop iteration to produce updates of $\mathbf{C}$ based on the newly formed time series. Each update of $\mathbf{C}$ improves the estimates of the missing data points by providing a new set of EOFs and PCs that allow one to recompute $r_{\ell 1}(t^*)$, the first RC, at the missing epochs.

Following Kondrashov and Ghil (2006), we used the normalized root-mean-square error (NRMSE), labeled here σ_inner, to define a convergence criterion for successive iterates of this inner loop. Applied to $r_{\ell 1}(t^*)$, this criterion is

$$\sigma_\mathrm{inner} := \frac{1}{\overline{r_{\ell 1}(t_j^*)}} \left(\frac{\sum_{j=1}^{n^*} \left(r_{\ell 1}^{(-)}(t_j^*) - \overline{r_{\ell 1}(t_j^*)} \right)^2}{n^*} \right)^{1/2} \leq 0.25\,; \tag{9}$$

here n^* are the number of epochs missing data points, $r_{\ell 1}^{(-)}(t_j^*)$ are the penultimate estimates, and $\overline{r_{\ell 1}(t_j^*)}$ is the average value of the estimated missing data points.

Once the convergence criterion (9) is met for $r_{\ell 1}(t^*)$ with $k = 1$ and $\ell = 1, ..., D$, we run a new series of outer-loop iterations; each of these follows the scheme described above for the

inner loop, but with increasing values of $k = 1, \ldots, k_{\max}$ that correspond to an increasing number of RCs being used in the estimate at the missing points t^*. For $k \geq 2$, the estimated values of the missing data points correspond to $\sum_{k=1}^{k'} r_{\ell k}(t_j^*)$. The choice of the maximum number $k_{\max}$ of RCs used to produce estimates of missing data points relies on a trade-off between the computational time required to run the gap filling algorithm and the maximum number of modes exploited to fill the gaps. Here we chose to use $k_{\max} = 10$. Examples of M-SSA gap-filling results using various values of M are displayed in supplementary Figure S2

Selecting the optimal parameters and gap filling results. We choose now to apply the gap filling algorithm to each pixel of an InSAR scene individually, while using simultaneously vertical and east–west displacement components. The scheme described above requires choosing two parameters: the window width M and of the number of modes $k_{\max}$ that determines the efficiency of the gap filling algorithm. Here, we wish the optimal pair of parameters (M_0, k_0) to produce the best estimates of the missing data, while minimizing the NRMSE, denoted now by σ_{outer}, between the variance of the original time series with the missing points and the estimated one that includes the values $r_{k\ell}(t^*)$. Using the optimal parameter pair (M_0, k_0) produces, therefore, time series that are as close as possible to the original time series in terms of their respective variances.

Since the means of the two series, with and without the gaps, are guaranteed by the methodology to be the same, this criterion ensures that the first- and second-order statistical properties of the estimated time series, with the gaps filled, are as close as possible to those of the original one. Note that this criterion differs from the one used in the three papers that introduced the M-SSA–based gap filling methodology (Kondrashov et al., 2005; Kondrashov & Ghil, 2006; Kondrashov et al., 2010); see supplementary Text S4 and Figure S3.

Two examples of the M-SSA gap filling algorithm's performance are displayed in Figure 4. They illustrate the results of this algorithm applied to two sets of time series that include the vertical and East–West displacements captured at the pixels represented by the white triangle and the gray filled circle in Figure 2; these pixels are located at coordinates $(-90.6129, 14.3684)$ and $(-90.6082, 14.3546)$, respectively.

Figure 4a shows how the NRMSE — which reflects the difference in variance between the original dataset and the gap-filled time series — varies as a function of the window width M and of the number k of modes used. The time series at pixel $(-90.6129, 14.3684)$ are optimally filled using $(M_0, k_0) = (25, 8)$, while the time series at pixel $(-90.6082, 14.3546)$ are optimally filled using $(M_0, k_0) = (50, 10)$. Gray dots in Figure 4b show the values of the estimated missing data points for the selected time series. Maps of optimal values of the parameters (M, k) are displayed in the supplementary materials for selected pixels together with their frequency distributions (Figure S4).

4.3 Decomposition of the InSAR time series with M-SSA

4.3.1 Applying M-SSA to large datasets

Now that we have obtained time series with a constant sampling interval, we use M-SSA to decompose them into their common modes of spatio-temporal variability. Here we present a way to apply M-SSA to analyze large datasets. Groth et al. (2016) introduced the approach presented herein that allows one to reduce the computational burden of the problem at hand. It is suitable when $D \gg N$, i.e., when the number of time series one wishes to analyze simultaneously using M-SSA is much larger than the number of data points constituting each of the series, as is the case for the InSAR datasets.

The interpolated InSAR time series of length $N = 1038$ are first projected onto spatial EOFs (S-EOFs) by classical PCA, i.e., following the steps in Section 4.1 and Eq. (2), with $M = 1$, to obtain $L = N = 1038$ spatial PCs (S-PCs). Since the common PCA exploits

solely spatial correlations between time series, the outputs of this step are referred to as S-EOFs and S-PCs. Let us denote the S-PCs by $\mathbf{y}_k$ and the S-EOFs by $\mathbf{e}_k$ so that, using Eq. (6), $\mathbf{y}_k = \mathbf{x}\mathbf{e}_k$.

The S-PCs $\mathbf{y}_k$ are then used as input channels for the subsequent M-SSA analysis. Following again the steps described in Section 4.1, we first create the matrix $\mathbf{Y} = (\mathbf{Y}_1, ..., \mathbf{Y}_l, ..., \mathbf{Y}_L)$, where each $\mathbf{Y}_k$ contains the S-PC $\mathbf{y}_k$ and its M lagged copies. One can show that the M-SSA analysis performed using $\mathbf{Y}$ provides, up to a sign, the same singular spectrum, EOFs and PCs as the M-SSA analysis performed using $\mathbf{X}$ (see supplementary Texts S5 and S6). The RCs $r_{lk}(t)$ of the time series composing the InSAR datasets can be obtained using:

$$\mathbf{r}_k = \mathbf{r}_k^{(Y)}\mathbf{e}' \tag{10}$$

where $\mathbf{r}^{(Y)}$ are the reconstructed components of the S-PCs. This approach reduces the computational cost of applying M-SSA analysis on very large datasets: instead of using directly D time series corresponding to pixels composing InSAR maps as input channels for M-SSA, we use the much smaller number of $L = N$ S-PCs.

4.3.2 Choice of window width parameter M and time series normalization

The key M-SSA parameter is M, which governs the maximum time lag $M\tau_\mathrm{s}$ by which the time series are delayed in order to compute the lag-covariances that form the elements of $\mathbf{C}^V$ and $\mathbf{C}^P$. A practical rule of thumb that seems to work well for geodetic time series is to choose a value of M so that $M\tau_\mathrm{s}$ corresponds roughly to one year (Walwer et al., 2016; Prevost et al., 2019). This provides a good separation between seasonal patterns of deformation — for which oscillations with an annual period and their harmonics capture a large part of the variance — and signals related to other geophysical processes. Here we use $M = 200$, so that the maximum lag is $M\tau_\mathrm{s} = 200 \times 2 = 400$ days.

Note that there is a trade-off associated with the choice of M. Using larger M-values allows for the extraction of modes of longer period and often allows to better unravel the different types of signals contained within a set of time series. Larger values of M, however, also imply fewer data points composing the rows of $\mathbf{X}$ or $\mathbf{Y}$, which have $N - M + 1$ elements each, and therefore fewer data points serving to estimate the lag-covariances matrix.

Before applying M-SSA, it is beneficial to center the data and normalize each time series by its standard deviation. The resulting time series have, therefore, zero mean and unit variance. In general, it is also useful to remove the linear trend from each time series, as these trends often account for a large part of the variance. Removing them allows one to focus the analysis on the nonlinear temporal patterns that contribute to the variability of interest.

4.3.3 The eigenspectrum and the principal components (PCs)

Here the vertical and horizontal components of the displacements are analyzed separately in order to stress their differences. Alternatively, one can also choose to analyze all available components simultaneously; see supplementary materials Text S7 and Figures S5-S6.

M-SSA offers a compression of the information shared across the time series that are being analyzed simultaneously. Sparse representation of information is provided by the eigenspectrum — i.e., the leading extracted eigenvalues $\{\lambda_k : k = 1, \ldots, K\}$, with $K \ll LM$, sorted in decreasing order — together with the associated EOFs $\{\mathbf{E}_k : k = 1, \ldots, K\}$ — and the corresponding PCs from (6). As an example, the 20 largest eigenvalues, as well as the first eight leading PCs extracted from the vertical and horizontal components of the displacements, are displayed in Figure 5a.

The eigenvalues in the top panels of Figure 5a are normalized by the total variance of the corresponding dataset obtained by summing all of them. Normalized in this way, the λ_k's correspond to the proportion of variance accounted for by the temporal modes of variability and captured by the corresponding PCs. As such, the first eigenvalue in Figure 5a for the vertical displacement is equal to $\simeq 0.13$ while for the east–west component it is equal to $\simeq 0.04$. In other words, the corresponding PCs#1 displayed below describe a mode of temporal variability that accounts for 13% and 4% of the total variance for the vertical and east–west displacements, respectively.

Several modes of temporal variability can be distinguished from the M-SSA results. Some PCs displayed in Figure 5a, such as PCs#1,2 and PCs#4,5 for instance, are oscillatory. Oscillatory modes extracted using M-SSA appear most often as pairs of eigenvalues having nearly equal values, while the corresponding eigenvectors and PCs are in phase quadrature (Vautard & Ghil, 1989; Ghil et al., 2002). They can be seen as nonlinear counterparts of a pair of sine and cosine functions of a given period. The advantage of M-SSA is that using these classical harmonic functions in Fourier analysis requires more than one (sine, cosine) pair to account for amplitude and phase modulation of an oscillatory signal, while one pair of M-SSA oscillatory components can do the same without additional components — hence the sparse representation provided by M-SSA (Ghil et al., 2002; Walwer et al., 2016).

Amplitude modulation in an oscillatory pair is well illustrated, for example, by PCs#4,5 in Figure 5a, extracted from the vertical component and displaying reduced amplitude between roughly year 2018 and year 2020. Importantly, since M-SSA is data adaptive, the period of these oscillations does not need to be determined a priori, an advantage over methods relying on adjusting prescribed harmonic functions to time series.

Contrary to the PCs mentioned above, PC#3 in Figure 5a is not oscillatory for either the horizontal or the vertical displacements. They describe long-periodic nonlinear trends that account for 6% and 3% of total variance, respectively.

4.3.4 Combining M-SSA and spectral analysis

M-SSA can be integrated very well with power spectrum–based analysis. First, M-SSA eigenvalues are sorted according to the dominant frequency f of the corresponding PCs, as suggested by Allen and Smith (1996) and commonly done for meteorological, oceanographic, and climatic time series (e.g., Ghil et al., 2002; Groth & Ghil, 2015). Such a representation is displayed in Figure 5b. The eigenvalues sorted in this manner read similarly to a power spectrum and show the frequencies that contribute the most to the temporal variability of an ensemble of time series analyzed simultaneously with M-SSA.

For example, the oscillatory pair formed by PC#1 and PC#2 in Figure 5a for the vertical component has dominant frequency $f = 1$ cy/yr and corresponds to seasonal annual oscillations; its pair of eigenvalues is therefore plotted at $f = 1$ cy/yr in the top left panel of Figure 5b.

Pairs formed by PCs#4,5 for the vertical component of the two datasets have a dominant frequency of 2 cy/yr. Modes of higher frequencies seem to involve harmonics of the annual oscillations. For example, a significant part of the variance is captured by oscillatory modes with dominant frequencies around 3 cycles per year. Interestingly both components also exhibit significant variance at frequencies 6.8 and 5.8 cycles per year.

Although the vertical and horizontal components are analyzed independently, they possess PCs having similar dominant frequencies. For example, the PCs reflecting the nonlinear trend display dominant frequencies around 0.3 cycle per year regardless of the component, presumably a subharmonic of the seasonal cycle.

Differences can also be noted, though, between the spectral content of the two components of the displacement at the same site. The vertical component is dominated by annual and semiannual oscillations, while the horizontal displacements do not exhibit oscillatory PCs having those periods. For the horizontal displacement, the lowest frequency captured by oscillatory PCs is 1.5 cycles per year.

5 Producing filtered maps of displacements

The previous sections focused on the temporal characteristics of the modes extracted by M-SSA analysis. We now present results revealing the spatial structure of these modes.

We compute reconstructions of the signals associated with the extracted modes, for each pixel, using Equation (8). Examples of reconstructions of the nonlinear trend captured either by PCs#3 are displayed in Figure 6a, while examples of reconstructions of the nonlinear trend together with the dominant oscillatory modes are displayed in Figure 6b. M-SSA's ability to reconstruct signals recorded at each pixel can be exploited to produce filtered maps of displacements and to study the spatial patterns associated with the different M-SSA modes.

Using such an approach allows one to produce maps of the spatial patterns of seasonal deformation. Thus, Figures 7 and 8 displays the values of standard deviations of reconstructed seasonal oscillations and nonlinear trends at each pixel, for the vertical and horizontal component, respectively. The amplitude of the dominant seasonal displacement pattern displayed as the first caption of each Figure correlates well with the topography: the amplitudes are higher at higher elevations.

Maps of the spatial variability of the low-frequency modes, associated with the third PCs, are shown in the second captions of Figures 7 and 8. The nonlinear trends in both the vertical and horizontal have higher amplitudes at higher elevations, nearer to the volcano's summit. In addition, the high amplitudes of the nonlinear trends in both components coincides clearly with the lava flows formed during the 2010 and 2014 south flank eruptions; see yellow and green bands in Figure 1.

It is interesting to observe that some of the extracted oscillatory modes are associated to coherent and clear asymetries in their spatial patterns. For example, the oscillatory modes at frequency 5.8 cycles per year have higher amplitude on the West side of the volcanic edifice compare the East side for both components as displayed in the last captions of Figures 7 and 8.

6 Discussion

In this section, we discuss the physical aspects of the oscillatory modes and of the nonlinear trend extracted by the M-SSA methodology.

6.1 Geophysical meaning of the oscillatory modes

It is informative to compare the eigenvalues extracted from the InSAR time series and sorted according to the dominant frequency of the corresponding PCs with the frequency content of datasets reflecting the variability of the regional hydrology (Figure 9a–d). The comparison shows that M-SSA oscillatory modes extracted from the Sentinel-1 data have counterparts in the rainfall power spectrum, as well as in M-SSA oscillatory modes extracted from the GPS, EWH, and ZTD time series that were presented in Section 3.2.

The most significant pairs of oscillatory modes extracted from InSAR vertical displacements have dominant frequencies at 1, 2, 3, 6.8, and 5.8 cy/yr, in order of the variance accounted for; all of them correlate with frequency peaks in the rainfall power spectra (Figure 9a). The dominant frequencies of the oscillatory pairs extracted from InSAR East–West

displacements, ordered by variance, are 6.8, 3, 1.5 and 5.8 cy/yr; they also correlate with peaks in the rainfall power spectrum (Figure 9a).

Pairs of M-SSA oscillatory modes were extracted furthermore from the GPS, GACOS and EWH time series (Figures 9a–d). The observed trends in frequency content in Figures 9a–d display systematically an increase at around 6 cy/yr for all datasets except the EWH time series. This increase is particularly pronounced for the InSAR East–West displacements. While annual and semi-annual modes of oscillations are commonly extracted from geodetic datasets, higher-frequency modes are more rarely discussed and are often considered as not being significant. It is interesting to note that, in the present results, M-SSA components oscillating at around 6 cy/yr and 7 cy/yr account for a significant part of the data variance; they are consistently present in all time series analyzed independently herein, which strengthens our confidence in this finding. M-SSA analysis performed on the InSAR line-of-sight (LOS) time series also yield components around 6 cy/yr (supplementary Text S8 and Figure S7, S8 and S9).

The main question concerning the InSAR seasonal oscillations is whether they reflect actual deformation — caused either by water surface load or water pore pressure fluctuations — or seasonal variability induced by the tropospheric water vapor delay or by other artefacts (Yu et al., 2017; Larochelle et al., 2021). As pointed out already by Gonzalez-Santana et al. (2022b), the seasonal variability in the ZTD expected from the vapor content at Pacaya is of the same order of magnitude as the seasonal variability observed within the vertical Sentinel-1 time series with a peak-to-peak annual amplitude of approximately 40 mm; compare, for example, Figure 2b and the time series in Figure 3c.

The spatial patterns of the various oscillatory modes extracted from the GACOS time series, however, do not always correlate with the ones extracted from the vertical displacements. While all GACOS seasonal patterns correlate with the topography, this is not the case for the ones extracted from the InSAR datasets; compare Figures 7 and 8 with Figure 10. Thus, the spatial patterns associated with the M-SSA modes oscillating at 5.8 cy/yr for both vertical and East–West InSAR displacements, for example, show clear and coherent asymmetries between the East and West side of the Pacaya edifice, unlike the spatial patterns of the GACOS modes oscillating at the same frequency; see Figures 7 and 10.

Without further modeling of surface displacements caused by surface load and fluid pore pressure, it is difficult to completely rule out that part of the observed seasonal signals extracted by M-SSA from InSAR data is the result of actual deformation. While it seems that a significant part of the seasonal oscillations extracted from the vertical InSAR displacements is caused by tropospheric delay, in agreement with Gonzalez-Santana et al. (2022b), the various asymmetric spatial patterns presented in Figures 7 and 8 may suggest that part of the oscillatory signal results from actual displacement of the surface caused potentially by seasonal surface load or pore pressure fluctuations. These patterns could also results from other atmospheric artefacts that do not correlate with the topography of the Pacaya edifice, such as local tropospheric refraction not accounted for by global atmospheric models and GACOS.

6.2 Geophysical meaning of the nonlinear trend

As for the seasonal oscillations, the complementary datasets presented in Section 3.2 help us interpret the geophysical meaning of the InSAR nonlinear trend extracted with M-SSA. The GPS and GRACE time series present also one or more M-SSA long-periodic modes and the rainfall time series has significant power at frequency lower than 1 cy/yr. Like the ones extracted from the InSAR vertical and East–West displacements, the latter are characterized by power spectra with a frequency peak at roughly 0.3 cy/yr; see again Figure 9.

This common spectral feature suggests that the nonlinear trend present in the Sentinel-1 time series is the result of the regional hydrology's interannual variability. Hydrology-related interannual variability in deformation data has been observed elsewhere and it is often associated with deformations caused by either multiannual variations in groundwater content or in surface water load (e.g., King et al., 2007; Silverii et al., 2016; Larochelle et al., 2021).

The nonlinear trends extracted from the InSAR vertical and horizontal displacements are displayed in Figure 11a and are compared with the long-periodic temporal patterns extracted from the complementary datasets in Figures 11(b–d). First, it is interesting to note that, while having the same frequency content, the nonlinear trend within the InSAR vertical displacements is distinct from the one in the horizontal displacements (Figure 11a). A similar distinction is found between the vertical and horizontal components recorded by the GPS station GUAT in Figure 11b.

For both the InSAR and GPS vertical displacements the nonlinear trend exhibits a V-shape with a lowest value around 2018, while the east–west component exhibits an inflection point at this date. The V-shape in the nonlinear trend of the vertical displacement correlates well with the long-term trend of the daily rainfall that has a minimum in 2018 as well; see the left panels in Figures 11a,b,c. The nonlinear trend from the horizontal displacement correlates better with the detrended cumulative rainfall in the right panels of Figures 11a,b,c.

Silverii et al. (2016) reported very similar relationships between vertical and horizontal surface displacements, as well as daily and detrended cumulative rainfall in the southern Apennines. According to these authors, such an observation reflects the different responses of vertical and horizontal surface displacements to the hydrologically driven deformation processes. They suggest that the vertical displacements result mainly from deformation induced by the long-term variation in surface water loads, while horizontal displacements arise from subsurface deformation induced by variations of fluid pressure within a fluid-filled conductive fracture system.

The interannual trend constitutive of the regional EWH time series shows a maximum value in 2018 and a minimum value at the end of 2019 (Figure 11d). While this result should be interpreted carefully due to the large gap in GRACE time series from 2016 to 2018, the long-term fluctuations in the total water mass reflected by the EWH time series may be the cause of the observed deformation at Pacaya. It is interesting to note also that the peak value in the EWH time series is delayed by a few months with respect to the extrema in InSAR and GPS displacements, as well as to the daily rainfall.

In terms of spatial patterns, both vertical and East–West InSAR displacements show higher amplitude at higher elevation. This amplification also occurs within the clearly delimited area of the southward 2014 lava flow and, to a lesser extent, of the 2010 lava flow. One possible interpretation is that the response in terms of deformation of the lava flows to long-term hydrology is distinct from the adjacent structures composing the edifice due to difference in mechanical properties (Larochelle et al., 2021).

7 Conclusions

We presented herein the first M-SSA application to InSAR time series. M-SSA is first used iteratively to estimate the values of missing data points in order to produce an evenly sampled InSAR dataset. It is then applied to the resulting time series to extract modes of spatio-temporal variability.

M-SSA decomposes InSAR time series into pairs of oscillatory modes that reflect patterns of seasonal variations, superimposed on interannual nonlinear trends. The spatial characteristics associated with these two types of modes are distinct from each other. The seasonal amplitudes of both vertical and horizontal displacements either correlate with Pacaya

topography or show clear and coherent asymmetries between the East and West side of the edifice. The nonlinear trends have high amplitudes in the areas covered by the southern 2014 lava flow as well as around the summit and, to a lesser extent, within the 2010 lava flows when compared to their surroundings.

The various seasonal and interannual modes of variability extracted using M-SSA from InSAR data have counterparts in the regional daily rainfall, GPS, GRACE, and GACOS tropospheric delay time series. M-SSA is able to reliably extract annual and semi-annual oscillations, as well as higher-frequency harmonics that are rarely examined and discussed. The harmonic oscillations at roughly 6 cy/yr and 7 cy/yr, in particular, seem to account for a significant fraction of the variability of the regional water cycle. While geodetic annual and semi-annual oscillations are commonly mentioned, these higher harmonics are usually ignored. It would be, therefore, of interest to integrate these harmonics in a more systematic manner into the study of seasonal deformation patterns in order to understand their origins.

Without further modeling of the surface displacements due to water surface load and fluid pore pressure variations, it is difficult to draw more definitive conclusions about the importance and relative contributions of these processes in producing the observed seasonal and interannual InSAR variability. Combining the high spatial resolution provided by InSAR with the ability of M-SSA to decompose time series into seasonal oscillatory components and nonlinear trends opens up interesting opportunities to mine for information about volcanic and seismo-tectonic events, as well as to ascertain the source of seasonal and interannual deformation correlated with regional water cycles.

Acknowledgements

This work was supported through a NASA Earth Surface and Interior grant (80NSSC20K0490), issued through the Science Mission Directorate's Earth Science Division. CW and DW also acknowledge support from the National Science Foundation (EAR 1923943) and the College of Earth and Mineral Sciences at Penn State. JGS is supported by a Future Investigators in NASA Earth and Space Science and Technology (FINESST) grant (80NSSC20K1632). InSAR data processing was performed on The Pennsylvania State University's Institute for Computational and Data Sciences' Roar supercomputer. We made use of the GNU Parallel software to run some codes in parallel Tange (2022).

Data Availability Statement

All derived InSAR products, M-SSA OCTAVE (or MATLAB) codes as well as a demo reproducing results presented herein are publicly available through ScholarSphere repository service administered by both the University Libraries and Information Technology Services at Penn State. (https://scholarsphere.psu.edu/; doi:10.26207/606g-5s27; Walwer et al. (2023)). All the complementary data sets are available freely. The GPS time series can be accessed through the Nevada Geodetic Laboratory website (geodesy.unr.edu). The GRACE time series is available from https://thegraceplotter.com/. GACOS dataset is available from http://www.gacos.net/. The daily rainfall time series is available from https://doi.org/10.5067/TRMM/TMPA/3H/7.

Sentinel-1 dataset	
Time period	25/4/2015 to 28/12/2020 (2015.31-2020.99)
Number of data points in time series	429
Number of rows	675
Number of lines	715
Geographic center coordinates	90.6° W, 14.35°N
Reference point coordinates	90.636°W, 14.339° N
M-SSA gap filling	
New constant sampling interval (τ_s)	2 days
New number of data points N	1038
Values of window width parameter M tested	$[5 - 10 - 25 - 50 - 100]$
Maximum number of modes k_{max}	10
InSAR M-SSA decomposition of groups of pixels	
Maximum window width $M\tau_s$	$2 \times 200 = 400$ days
Number of coherent pixels analyzed simultaneously	3247

Table 1. Sentinel 1 dataset characteristics in Section 3, along with the main parameters for M-SSA gap filling in Section 4.2 and M-SSA data-adaptive decomposition in Section 4.3.

692 **Table**

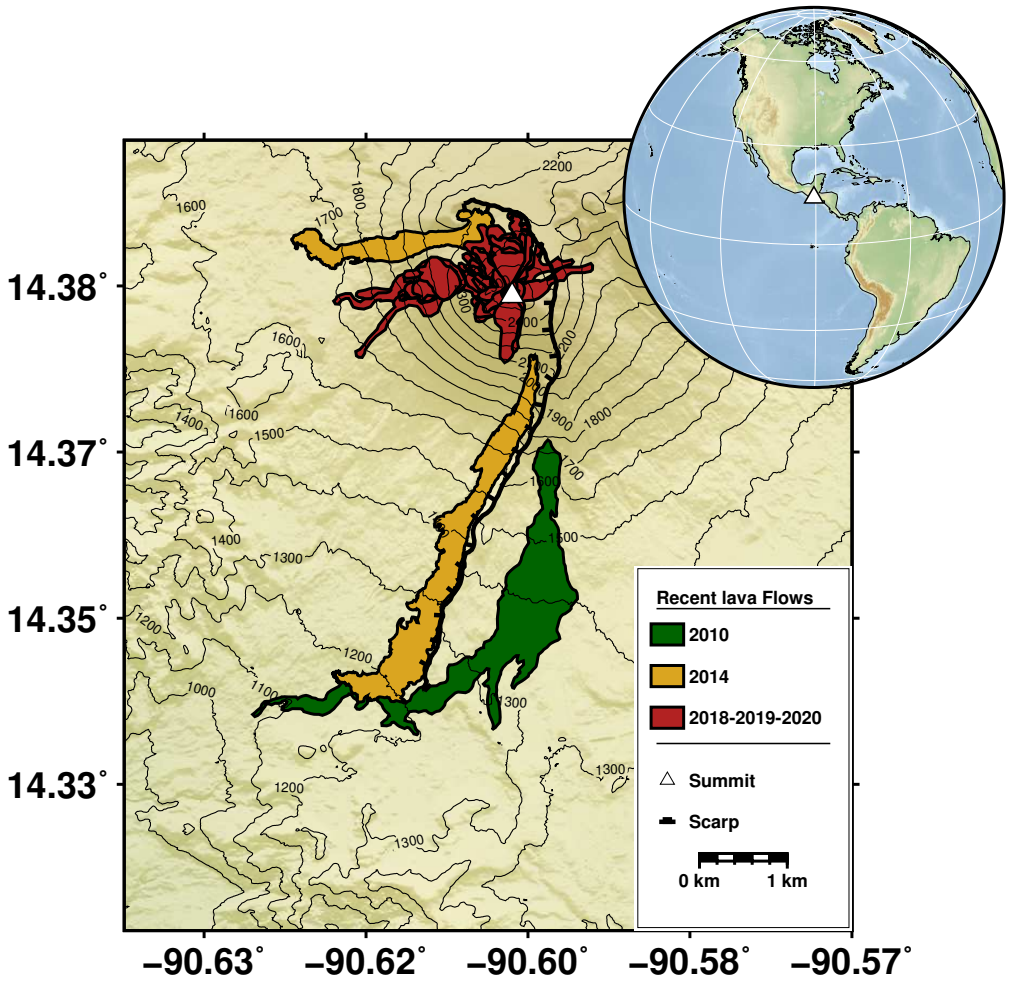

Figure 1. Topography of Pacaya Volcano, Guatemala. The green, yellow, and red polygons show the lava flows from the 2010, 2014, and 2018–2020 eruptions, respectively. The bold black line highlights a scarp from an ancestral collapse of the volcanic edifice.

693 ## Figures

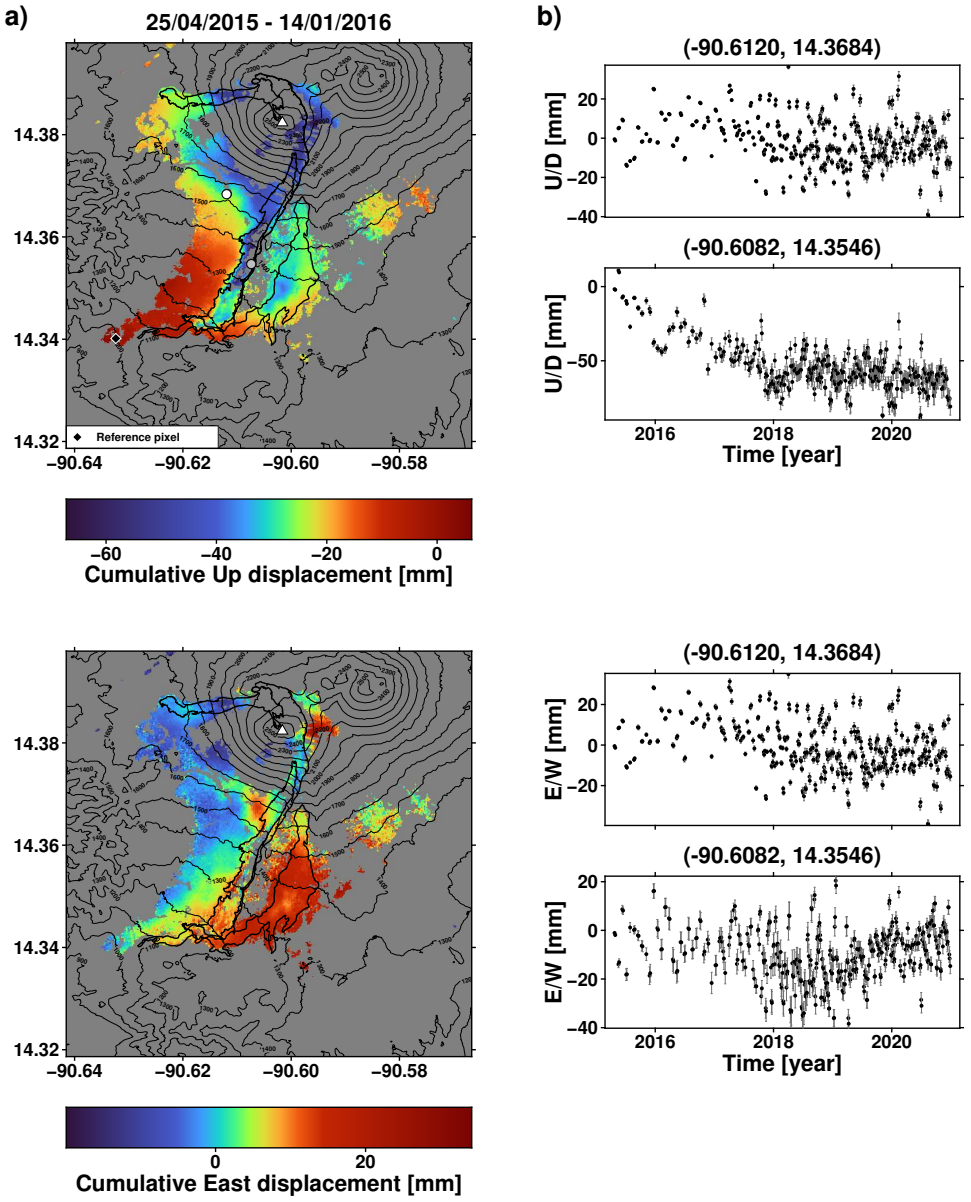

Figure 2. Sentinel-1 dataset for Pacaya volcano. a) Examples of two InSAR scenes showing cumulative up-down (top) and east-west (bottom) displacements from 25/04/2015 to 14/02/2016. White and gray open circles in the upper panel show pixel locations corresponding to the time series used to illustrate InSAR M-SSA applications in Sections 4.2 and 4.3. The black diamond shows the reference pixel location. b) Time series of up-down and east-west displacements associated with the pixels at the center of the two groups of white and gray open circles. The Cartesian coordinates of the center pixels are $(267, 267)$ for the white open circles and $(390, 308)$ for the gray open circles.

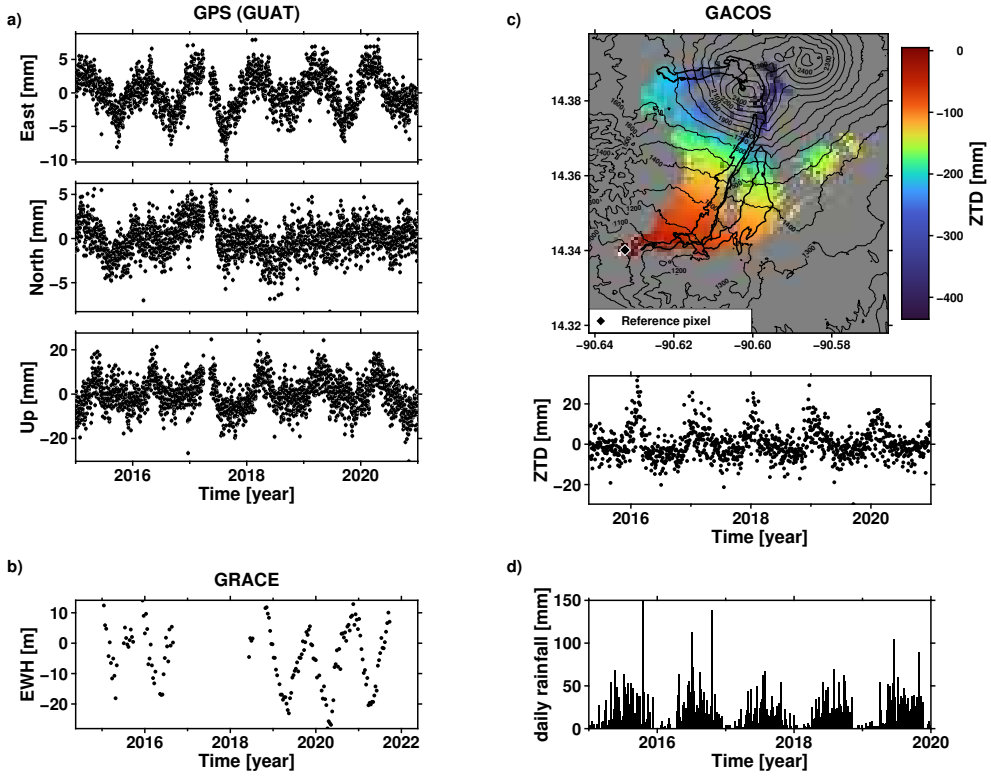

Figure 3. Complementary datasets. a) East and vertical component of the time series of GNSS position recorded at station GUAT (14.590°N −90.520° E) in Guatemala City, obtained from the Nevada Geodetic Laboratory (geodesy.unr.edu). b) Regional GRACE time series of equivalent water height (EWH) taken from CNES solutions and covering a rectangle above Guatemala; downloaded from `https://thegraceplotter.com/`. c) GACOS zenith tropospheric delay (ZTD) map at Pacaya corresponding to the date 14 January 2016. Below is an example of the ZTD time series at a given pixel. The black diamond shows the reference pixel location, which is the same as for the Sentinel 1 data in Figure 2a. d) Daily rainfall time series from from NASA/JAXA Tropical Rainfall Measurement Mission and Global Precipitation Measurement mission data at `https://doi.org/10.5067/TRMM/TMPA/3H/7`.

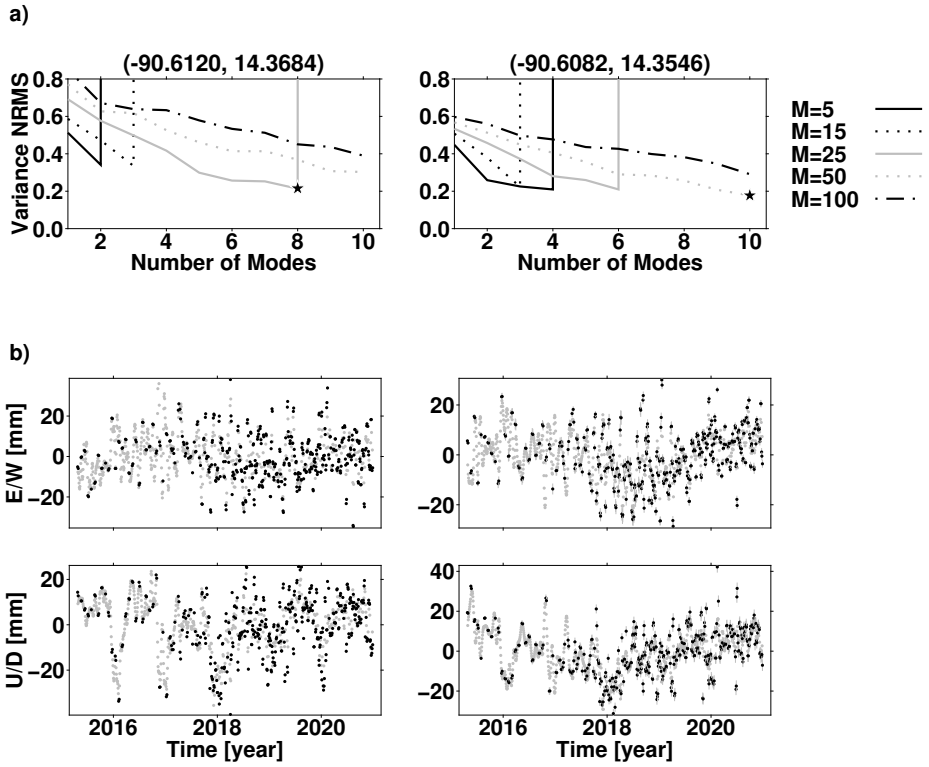

Figure 4. Results from the M-SSA gap filling algorithm. a) Selection of the optimal pair (M_0, k_0) of parameters that produce the best estimates of missing data points by minimizing the NRMSE between the original time series (black dots in panel (b)) and the new time series (black plus gray dots in (b)). This difference is computed between The optimal point $(NRMSE_0, k_0)$ is marked by the black star in each sub-panel. b) Original (black dots) and final (grey dots) time series. Grey dots correspond to the data points obtained with the M-SSA gap filling algorithm. The final uniform-sampling interval is $\tau_s = 2$ days.

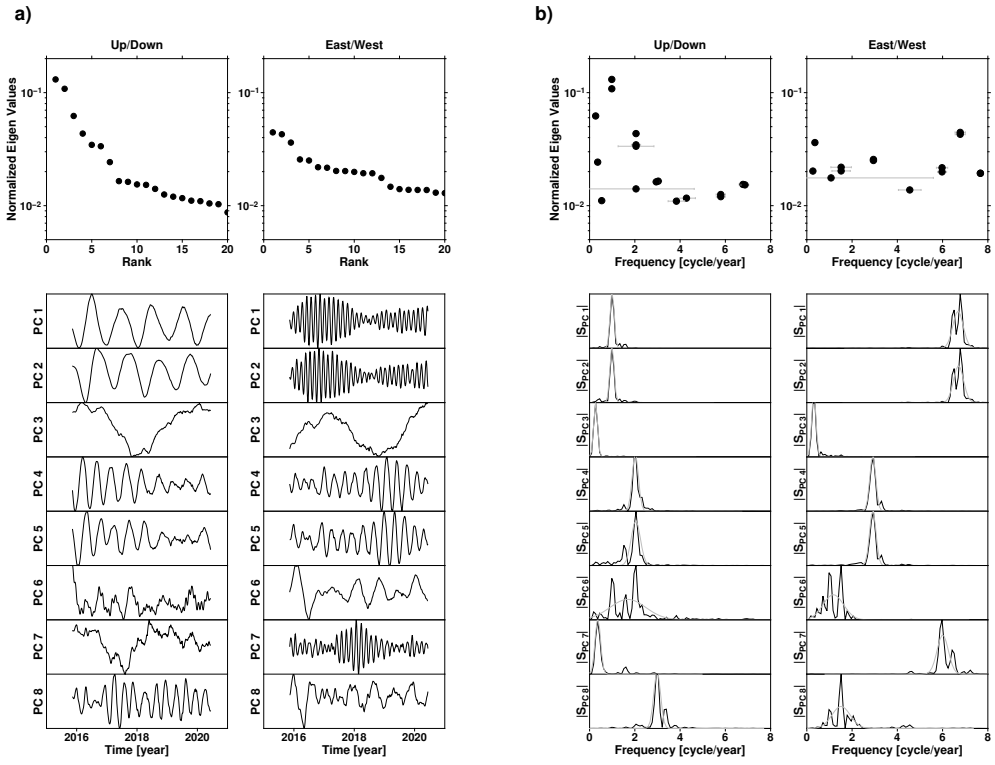

Figure 5. Examples of M-SSA decompositions of vertical and East-West InSAR time series. a) Upper panels display the normalized eigenvalues obtained using equation (4) and sorted in decreasing order of variance captured. Lower panels show the first 8 PCs obtained using equation (6). Note that oscillatory modes are characterized by pairs of nearly equal eigenvalues with their corresponding PCs in phase quadrature (Vautard & Ghil, 1989; Ghil et al., 2002); see for example PC1 and PC2 for both components. b) Spectral-domain representation of the M-SSA decomposition. Upper panels display the normalized eigenvalues obtained using equation (4) and sorted according to the dominant frequency of the associated PC. Lower panels show the power spectra of the 8 leading PCs and the associated Gaussian fit in frequency f (horizontal gray line).

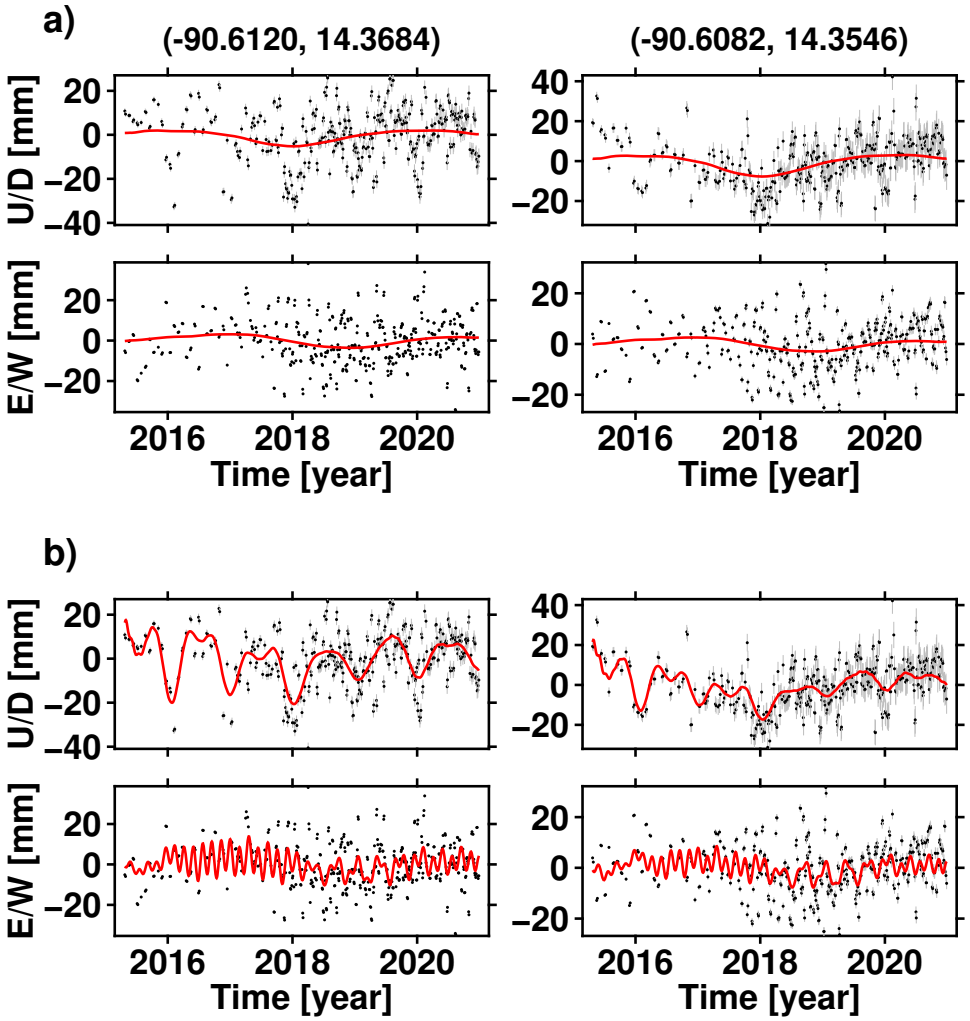

Figure 6. Examples of M-SSA reconstructions of signals at two different pixel locations, (-90.6120, 14.3684) in the figure's left column and (-90.6082, 14.3546) in the figure's right column. a) Nonlinear trend reconstructions. b) Reconstructions of the nonlinear trend together with the first four oscillatory modes.

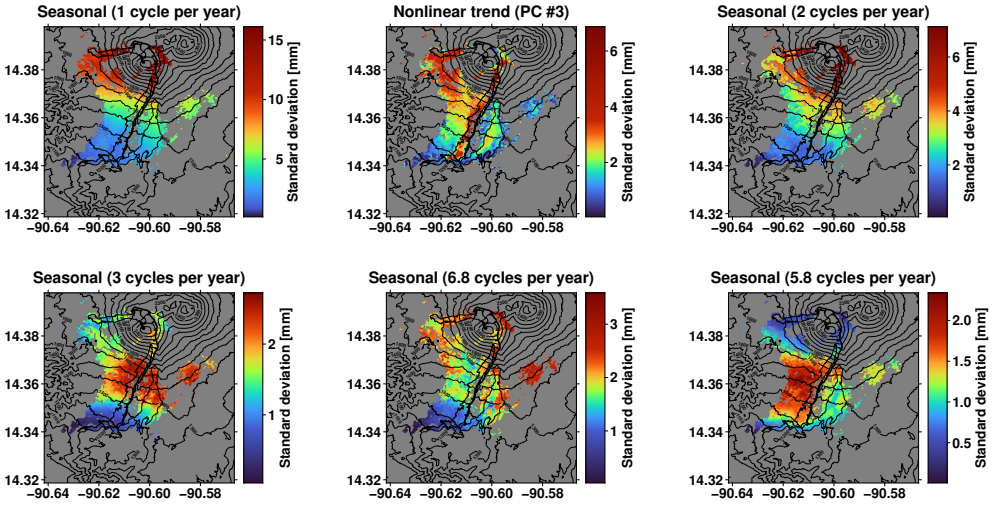

Figure 7. Spatial patterns of the dominant M-SSA modes extracted from the vertical component.

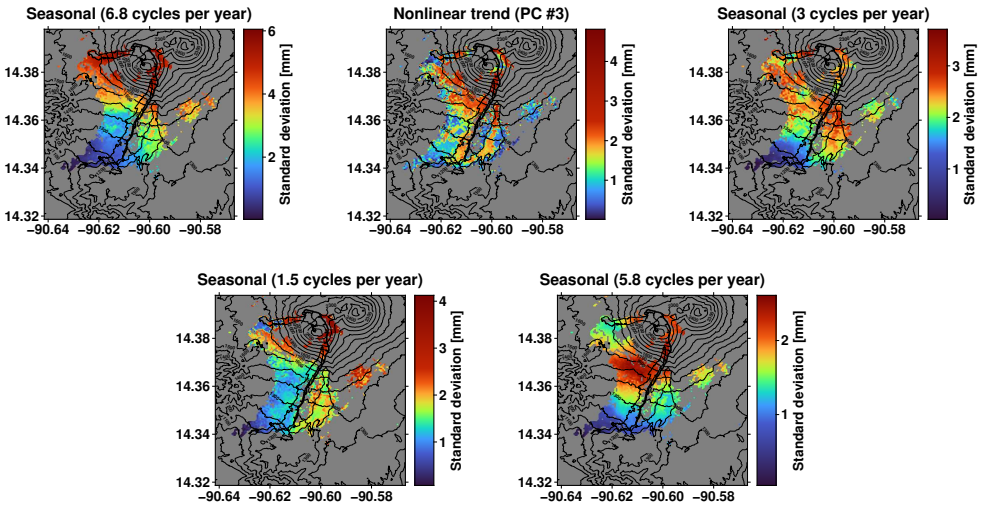

Figure 8. Spatial patterns of the dominant M-SSA modes extracted from the horizontal component.

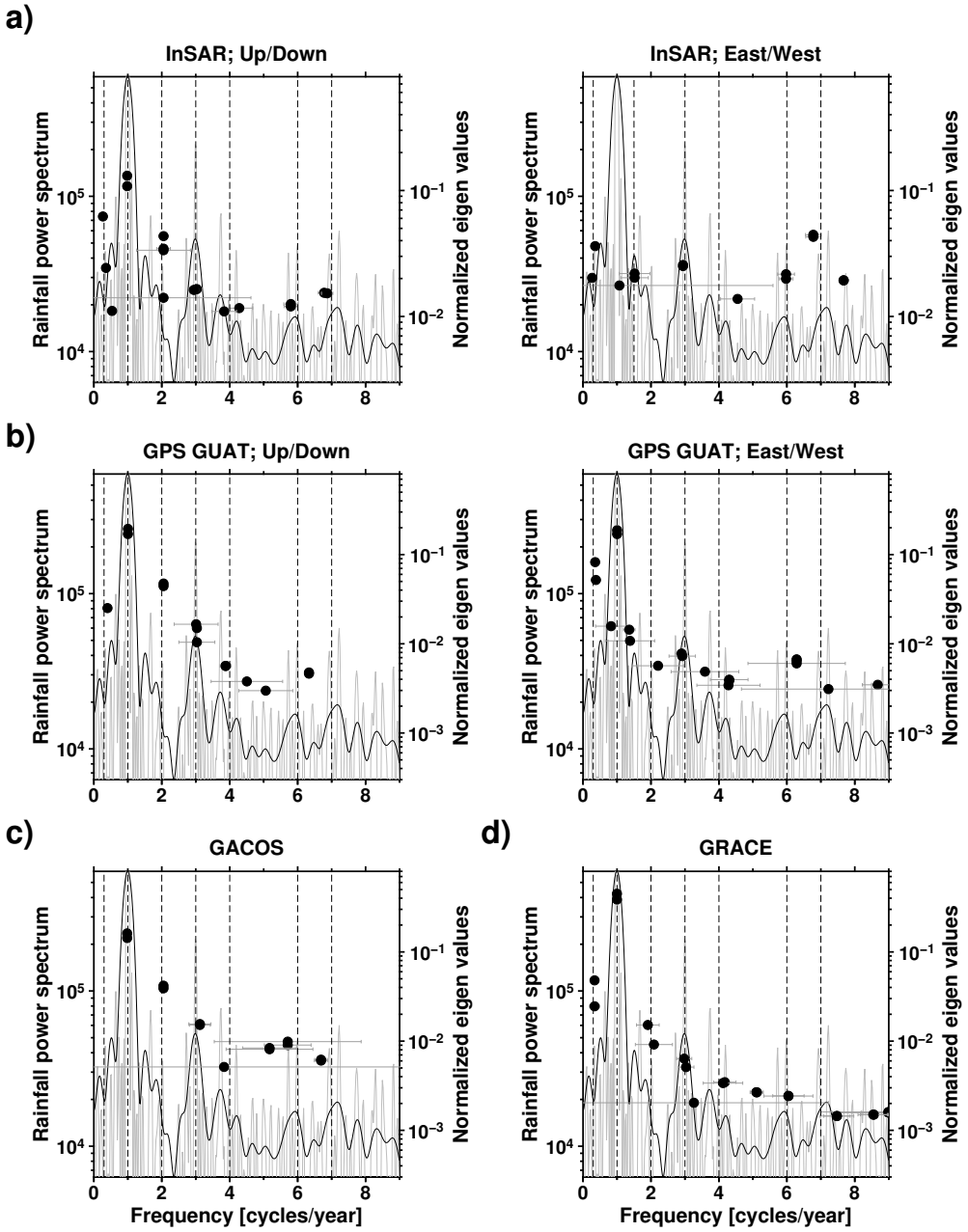

Figure 9. Spectral analysis of daily rainfall data compared to M-SSA eigenvalues (filled circles) plotted vs. dominant frequency for the InSAR time series and the complementary datasets presented in Section 3.2. (a) InSAR and (b) GPS, both vertical and horizontal; (c) GACOS and (d) GRACE. The rainfall power spectrum is estimated using a raw correlogram (gray curve) and a lag-window estimate with a Bartlett window (black curve) (e.g., Ghil et al., 2002). The vertical dashed lines highlight the frequencies at 0.3, 1, 2, 3, 6 and 7 cy/yr.

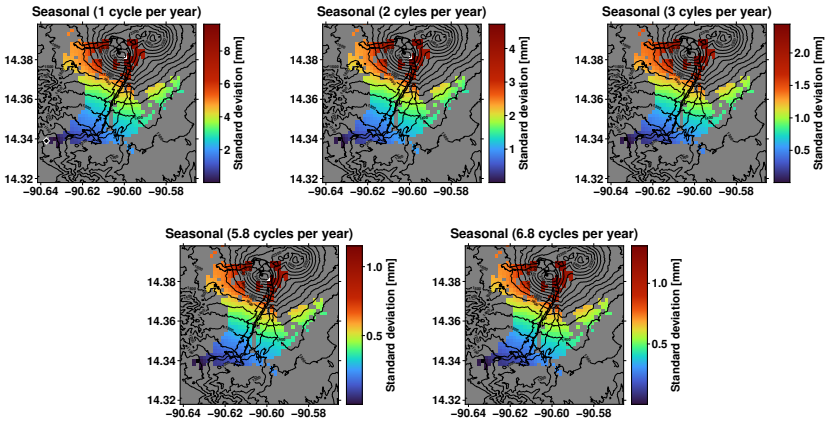

Figure 10. Spatial patterns of the dominant M-SSA modes extracted from GACOS ZTD dataset.

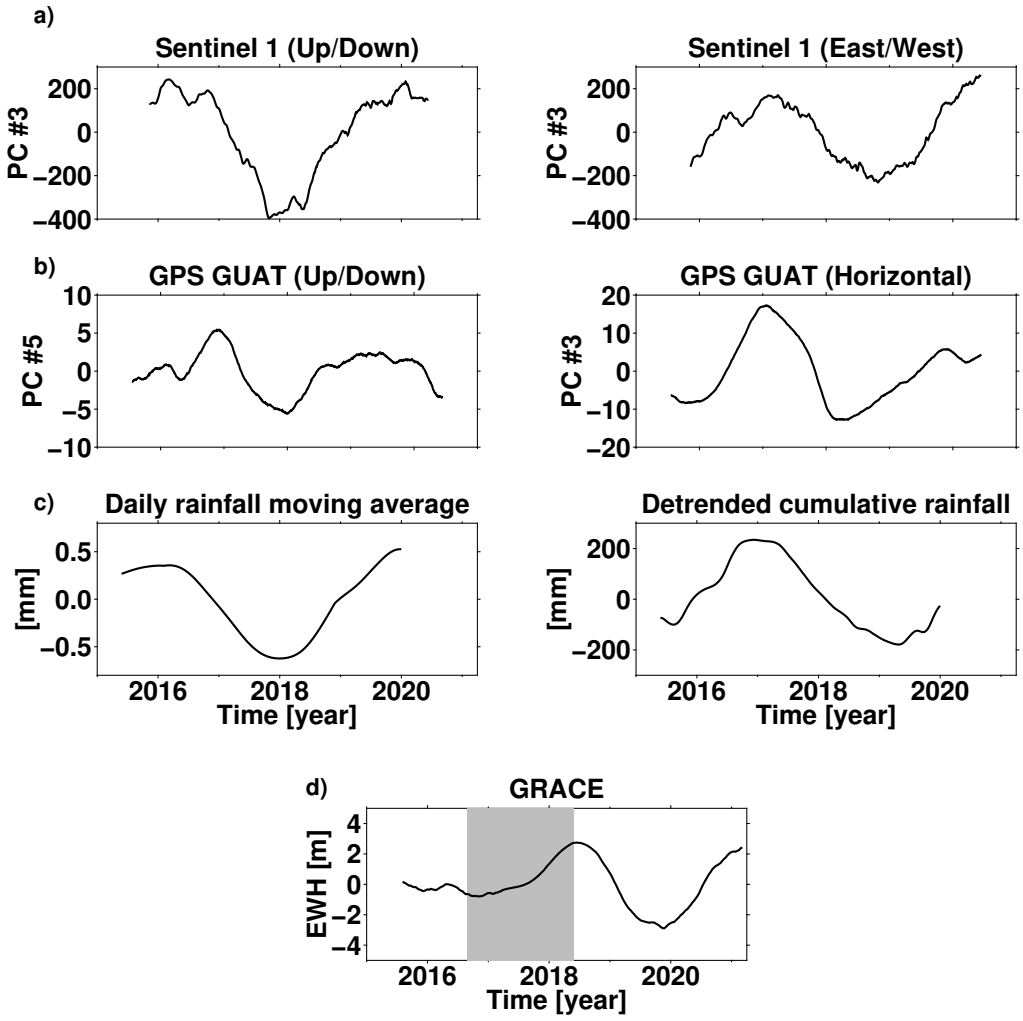

Figure 11. Interannual variability of the InSAR and complementary datasets. a) Typical shape of the nonlinear trends extracted with M-SSA for vertical (left) and East-West (right) InSAR displacements. b) Shape of the nonlinear trend extracted with M-SSA for Vertical (left) and Horizontal (right) GPS displacements recorded in Guatemala City. c) Left: interannual variability of the daily rainfall obtained by applying a moving average and M-SSA and right: detrended cumulative rainfall; d) Interannual variability extracted from GRACE EWH regional time series using M-SSA. The grey area displays the gap of missing data point in GRACE time series.

References

Alessio, S. M. (2016). *Digital Signal Processing and Spectral Analysis for Scientists: Concepts and Applications*. Springer. Retrieved from http://www.springer.com/us/book/9783319254661 (Ch. 12. Singular Spectrum Analysiss (SSA), pp. 537–571)

Allen, M. R., & Robertson, A. W. (1996). Distinguishing modulated oscillations from coloured noise in multivariate datasets. *Climate dynamics*, *12*, 775–784.

Allen, M. R., & Smith, L. A. (1996). Monte Carlo SSA: Detecting irregular oscillations in the presence of colored noise. *J. Climate*, *9*, 3373–3404. doi: 10.1175/1520-0442(1996)009⟨3373:MCSDIO⟩2.0.CO;2

Anantrasirichai, N., Biggs, J., Albino, F., Hill, P., & Bull, D. (2018, August). Application of Machine Learning to Classification of Volcanic Deformation in Routinely Generated InSAR Data. *Journal of Geophysical Research: Solid Earth*. Retrieved 2021-11-04, from http://doi.wiley.com/10.1029/2018JB015911 doi: 10.1029/2018JB015911

Béjar-Pizarro, M., Ezquerro, P., Herrera, G., Tomás, R., Guardiola-Albert, C., Hernández, J. M. R., ... Martínez, R. (2017). Mapping groundwater level and aquifer storage variations from insar measurements in the madrid aquifer, central spain. *Journal of Hydrology*, *547*, 678–689.

Bettinelli, P., Avouac, J.-P., Flouzat, M., Bollinger, L., Ramillien, G., Rajaure, S., & Sapkota, S. (2008). Seasonal variations of seismicity and geodetic strain in the himalaya induced by surface hydrology. *Earth and Planetary Science Letters*, *266*(3-4), 332–344.

Biggs, J., Lu, Z., Fournier, T., & Freymueller, J. T. (2010). Magma flux at okmok volcano, alaska, from a joint inversion of continuous gps, campaign gps, and interferometric synthetic aperture radar. *Journal of Geophysical Research: Solid Earth*, *115*(B12).

Blewitt, G., Hammond, W. C., & Kreemer, C. (2018). Harnessing the GPS data explosion for interdisciplinary science. *Eos*, *99*(10.1029), 485.

Broomhead, D. S., & King, G. P. (1986). Extracting qualitative dynamics from experimental data. *Physica D: Nonlinear Phenomena*, *20*(2-3), 217–236.

Chanard, K., Fleitout, L., Calais, E., Rebischung, P., & Avouac, J. (2018, April). Toward a Global Horizontal and Vertical Elastic Load Deformation Model Derived from GRACE and GNSS Station Position Time Series. *Journal of Geophysical Research: Solid Earth*, *123*(4), 3225–3237. Retrieved 2021-11-04, from https://onlinelibrary.wiley.com/doi/abs/10.1002/2017JB015245 doi: 10.1002/2017JB015245

Chanard, K., Métois, M., Rebischung, P., & Avouac, J.-P. (2020). A warning against over-interpretation of seasonal signals measured by the global navigation satellite system. *Nature communications*, *11*(1), 1–4.

Cohen-Waeber, J., Bürgmann, R., Chaussard, E., Giannico, C., & Ferretti, A. (2018). Spatiotemporal patterns of precipitation-modulated landslide deformation from independent component analysis of insar time series. *Geophysical Research Letters*, *45*(4), 1878–1887.

Craig, T. J., Chanard, K., & Calais, E. (2017, December). Hydrologically-driven crustal stresses and seismicity in the New Madrid Seismic Zone. *Nature Communications*, *8*(1), 2143. Retrieved 2021-11-04, from http://www.nature.com/articles/s41467-017-01696-w doi: 10.1038/s41467-017-01696-w

Dalaison, M., & Jolivet, R. (2020). A kalman filter time series analysis method for insar. *Journal of Geophysical Research: Solid Earth*, *125*(7), e2019JB019150.

Ebmeier, S. K. (2016, December). Application of independent component analysis to multitemporal InSAR data with volcanic case studies: ICA Analysis of InSAR Data. *Journal of Geophysical Research: Solid Earth*, *121*(12), 8970–8986. Retrieved 2021-11-04, from http://doi.wiley.com/10.1002/2016JB013765 doi: 10.1002/2016JB013765

Ebmeier, S. K., Biggs, J., Mather, T. A., & Amelung, F. (2013). Applicability of insar to tropical volcanoes: insights from central america. *Geological Society, London, Special Publications*, *380*(1), 15–37.

Gaddes, M., Hooper, A., & Bagnardi, M. (2019). Using machine learning to automatically detect volcanic unrest in a time series of interferograms. *Journal of Geophysical*

Research: Solid Earth, *124*(11), 12304–12322.

Ghil, M., Allen, M. R., Dettinger, M. D., Ide, K., Kondrashov, D., Mann, M. E., ... others (2002). Advanced spectral methods for climatic time series. *Reviews of Geophysics*, *40*(1), 3–1. Retrieved 2014-12-08, from http://onlinelibrary.wiley.com/doi/10.1029/2000RG000092/full

Ghil, M., & Vautard, R. (1991). Interdecadal oscillations and the warming trend in global temperature time series. *Nature*, *350*, 324–327.

Gonzalez-Santana, J., & Wauthier, C. (2021). Unraveling long-term volcano flank instability at Pacaya Volcano, Guatemala, using satellite geodesy. *Journal of Volcanology and Geothermal Research*, *410*, 107147. Retrieved 2021-11-04, from https://linkinghub.elsevier.com/retrieve/pii/S0377027320305837 doi: 10.1016/j.jvolgeores.2020.107147

Gonzalez-Santana, J., Wauthier, C., & Burns, M. (2022a). *A conceptual model for the initiation of flank creep at Pacaya Volcano, Guatemala.*

Gonzalez-Santana, J., Wauthier, C., & Burns, M. (2022b). Links between volcanic activity and flank creep behavior at Pacaya Volcano, Guatemala. *Bulletin of Volcanology*, *84*(9), 1–13.

Groth, A., Feliks, Y., Kondrashov, D., & Ghil, M. (2016). Interannual variability in the North Atlantic ocean's temperature field and its association with the wind stress forcing. *Journal of Climate*, *30*. (published online) doi: 10.1175/jcli-d-16-0370.1

Groth, A., & Ghil, M. (2015). Monte Carlo singular spectrum analysis (SSA) revisited: Detecting oscillator clusters in multivariate datasets. *Journal of Climate*, *28*(19), 7873–7893.

Gualandi, A., Perfettini, H., Radiguet, M., Cotte, N., & Kostoglodov, V. (2017, June). GPS deformation related to the M_w 7.3, 2014, Papanoa earthquake (Mexico) reveals the aseismic behavior of the Guerrero seismic gap. *Geophysical Research Letters*, *44*(12), 6039–6047. Retrieved 2021-11-04, from https://onlinelibrary.wiley.com/doi/10.1002/2017GL072913 doi: 10.1002/2017GL072913

Gualandi, A., Serpelloni, E., & Belardinelli, M. E. (2016, April). Blind source separation problem in GPS time series. *Journal of Geodesy*, *90*(4), 323–341. Retrieved 2021-11-04, from http://link.springer.com/10.1007/s00190-015-0875-4 doi: 10.1007/s00190-015-0875-4

Hooper, A., Bekaert, D., Spaans, K., & Arıkan, M. (2012). Recent advances in sar interferometry time series analysis for measuring crustal deformation. *Tectonophysics*, *514*, 1–13.

Hyvärinen, A., & Oja, E. (2000, June). Independent component analysis: algorithms and applications. *Neural Networks*, *13*(4-5), 411–430. Retrieved 2021-11-04, from https://linkinghub.elsevier.com/retrieve/pii/S0893608000000265 doi: 10.1016/S0893-6080(00)00026-5

Jolivet, R., Agram, P. S., Lin, N. Y., Simons, M., Doin, M.-P., Peltzer, G., & Li, Z. (2014). Improving insar geodesy using global atmospheric models. *Journal of Geophysical Research: Solid Earth*, *119*(3), 2324–2341.

Jolivet, R., Grandin, R., Lasserre, C., Doin, M.-P., & Peltzer, G. (2011). Systematic InSAR tropospheric phase delay corrections from global meteorological reanalysis data. *Geophysical Research Letters*, *38*(17).

Jolivet, R., Lasserre, C., Doin, M.-P., Peltzer, G., Avouac, J.-P., Sun, J., & Dailu, R. (2013). Spatio-temporal evolution of aseismic slip along the haiyuan fault, china: Implications for fault frictional properties. *Earth and Planetary Science Letters*, *377*, 23–33.

King, N., Argus, D., Langbein, J., Agnew, D., Bawden, G., Dollar, R., ... others (2007). Space geodetic observation of expansion of the san gabriel valley, california, aquifer system, during heavy rainfall in winter 2004–2005. *Journal of Geophysical Research: Solid Earth*, *112*(B3).

Kiyoo, M. (1958). Relations between the eruptions of various volcanoes and the deformations of the ground surfaces around them. *Earthq Res Inst*, *36*, 99–134.

Kondrashov, D., Feliks, Y., & Ghil, M. (2005). Oscillatory modes of extended Nile River

records (A.D. 622–1922). *Geophysical Research Letters*, *32*(10), L10702. Retrieved 2015-03-03, from http://onlinelibrary.wiley.com/doi/10.1029/2004GL022156/abstract doi: 10.1029/2004GL022156

Kondrashov, D., & Ghil, M. (2006). Spatio-temporal filling of missing points in geophysical data sets. *Nonlin. Processes Geophys.*, *13*(2), 151–159. Retrieved 2015-03-03, from http://www.nonlin-processes-geophys.net/13/151/2006/ doi: 10.5194/npg-13-151-2006

Kondrashov, D., Shprits, Y., & Ghil, M. (2010). Gap filling of solar wind data by singular spectrum analysis. *Geophysical Research Letters*, *37*(15), n/a–n/a. Retrieved 2014-12-07, from http://doi.wiley.com/10.1029/2010GL044138 doi: 10.1029/2010GL044138

Larochelle, S., Chanard, K., Fleitout, L., Fortin, J., Gualandi, A., Longuevergne, L., ... Avouac, J.-P. (2021). Understanding the geodetic signature of large aquifer systems: Example of the Ozark Plateaus in Central United States. *Journal of Geophysical Research: Solid Earth*.

Larochelle, S., Gualandi, A., Chanard, K., & Avouac, J. (2018, December). Identification and Extraction of Seasonal Geodetic Signals Due to Surface Load Variations. *Journal of Geophysical Research: Solid Earth*, *123*(12). Retrieved 2021-11-04, from https://onlinelibrary.wiley.com/doi/10.1029/2018JB016607 doi: 10.1029/2018JB016607

Li, Y., Bürgmann, R., & Taira, T. (2023). Spatiotemporal variations of surface deformation, shallow creep rate, and slip partitioning between the san andreas and southern calaveras fault. *Journal of Geophysical Research: Solid Earth*, *128*(1), e2022JB025363.

Lundgren, P., Liu, Z., & Ali, S. T. (2022). San Andreas fault stress change due to groundwater withdrawal in California's Central Valley, 1860–2010. *Geophysical Research Letters*, *49*(3), e2021GL095975.

Lundgren, P., Usai, S., Sansosti, E., Lanari, R., Tesauro, M., Fornaro, G., & Berardino, P. (2001). Modeling surface deformation observed with synthetic aperture radar interferometry at campi flegrei caldera. *Journal of Geophysical Research: Solid Earth*, *106*(B9), 19355–19366.

Massonnet, D., Briole, P., & Arnaud, A. (1995). Deflation of mount etna monitored by spaceborne radar interferometry. *Nature*, *375*(6532), 567–570.

Massonnet, D., & Feigl, K. L. (1998). Radar interferometry and its application to changes in the earth's surface. *Reviews of geophysics*, *36*(4), 441–500.

Okada, Y. (1985). Surface deformation due to shear and tensile faults in a half-space. *Bulletin of the seismological society of America*, *75*(4), 1135–1154.

Pinel, V., Poland, M., & Hooper, A. (2014, December). Volcanology: Lessons learned from Synthetic Aperture Radar imagery. *Journal of Volcanology and Geothermal Research*, *289*, 81–113. Retrieved 2021-11-04, from https://linkinghub.elsevier.com/retrieve/pii/S0377027314003084 doi: 10.1016/j.jvolgeores.2014.10.010

Prawirodirdjo, L., Ben-Zion, Y., & Bock, Y. (2006). Observation and modeling of thermoelastic strain in southern california integrated gps network daily position time series. *Journal of Geophysical Research: Solid Earth*, *111*(B2).

Preisendorfer, R. W. (1988). *Principal Component Analysis in Meteorology and Oceanography, compiled and edited by C. D. Mobley* (Vol. 17). Elsevier.

Prevost, P., Chanard, K., Fleitout, L., Calais, E., Walwer, D., van Dam, T., & Ghil, M. (2019, December). Data-adaptive spatio-temporal filtering of GRACE data. *Geophysical Journal International*, *219*(3), 2034–2055. Retrieved 2021-11-04, from https://academic.oup.com/gji/article/219/3/2034/5571817 doi: 10.1093/gji/ggz409

Riel, B., Simons, M., Agram, P., & Zhan, Z. (2014). Detecting transient signals in geodetic time series using sparse estimation techniques. *Journal of Geophysical Research: Solid Earth*, *119*(6), 5140–5160.

Rouet-Leduc, B., Jolivet, R., Dalaison, M., Johnson, P. A., & Hulbert, C. (2021). Autonomous extraction of millimeter-scale deformation in insar time series using deep learning. *Nature communications*, *12*(1), 1–11.

Schaefer, L., Di Traglia, F., Chaussard, E., Lu, Z., Nolesini, T., & Casagli, N. (2019). Monitoring volcano slope instability with synthetic aperture radar: A review and new data from pacaya (guatemala) and stromboli (italy) volcanoes. *Earth-science reviews*, *192*, 236–257.

Schaefer, L., Lu, Z., & Oommen, T. (2015). Dramatic volcanic instability revealed by insar. *Geology*, *43*(8), 743–746.

Silverii, F., d'Agostino, N., Métois, M., Fiorillo, F., & Ventafridda, G. (2016). Transient deformation of karst aquifers due to seasonal and multiyear groundwater variations observed by gps in southern apennines (italy). *Journal of Geophysical Research: Solid Earth*, *121*(11), 8315–8337.

Simons, M., & Rosen, P. (2007). Interferometric synthetic aperture radar geodesy. *Geodesy*, *3*, 391–446.

Stephens, K. J., Wauthier, C., Bussard, R. C., Higgins, M., & LaFemina, P. C. (2020). Assessment of mitigation strategies for tropospheric phase contributions to insar time-series datasets over two nicaraguan volcanoes. *Remote Sensing*, *12*(5), 782.

Sun, J., Wauthier, C., Stephens, K., Gervais, M., Cervone, G., La Femina, P., & Higgins, M. (2020, September). Automatic Detection of Volcanic Surface Deformation Using Deep Learning. *Journal of Geophysical Research: Solid Earth*, *125*(9). Retrieved 2021-11-04, from `https://onlinelibrary.wiley.com/doi/10.1029/2020JB019840` doi: 10.1029/2020JB019840

Tange, O. (2022). *GNU Parallel 20220522 ('NATO')* (Tech. Rep.). Retrieved from `https://doi.org/10.5281/zenodo.6570228` doi: 10.5281/zenodo.6570228

Vautard, R., & Ghil, M. (1989). Singular spectrum analysis in nonlinear dynamics, with applications to paleoclimatic time series. *Physica D: Nonlinear Phenomena*, *35*(3), 395–424. Retrieved 2014-12-07, from `http://www.sciencedirect.com/science/article/pii/0167278989900778`

Walwer, D., Calais, E., & Ghil, M. (2016, March). Data-adaptive detection of transient deformation in geodetic networks: DATA-ADAPTIVE GPS TIME SERIES ANALYSIS. *Journal of Geophysical Research: Solid Earth*, *121*(3), 2129–2152. Retrieved 2016-05-11, from `http://doi.wiley.com/10.1002/2015JB012424` doi: 10.1002/2015JB012424

Walwer, D., Ghil, M., & Calais, E. (2022). A data-based minimal model of episodic inflation events at volcanoes. front. *Earth Sci*, *10*, 759475.

Walwer, D., Gonzalez-Santana, J., Wauthier, C., Calais, E., & Ghil, M. (2023). *M-SSA for InSAR.* (Software and dataset) doi: 10.26207/606g-5s27

Wnuk, K., & Wauthier, C. (2017). Surface deformation induced by magmatic processes at pacaya volcano, guatemala revealed by insar. *Journal of Volcanology and Geothermal Research*, *344*, 197-211. Retrieved from `https://www.sciencedirect.com/science/article/pii/S0377027317303967` (Volcano Geodesy: Recent developments and future challenges) doi: https://doi.org/10.1016/j.jvolgeores.2017.06.024

Yu, C., Li, Z., & Penna, N. T. (2018). Interferometric synthetic aperture radar atmospheric correction using a gps-based iterative tropospheric decomposition model. *Remote Sensing of Environment*, *204*, 109–121.

Yu, C., Li, Z., Penna, N. T., & Crippa, P. (2018). Generic atmospheric correction model for interferometric synthetic aperture radar observations. *Journal of Geophysical Research: Solid Earth*, *123*(10), 9202–9222.

Yu, C., Penna, N. T., & Li, Z. (2017). Generation of real-time mode high-resolution water vapor fields from gps observations. *Journal of Geophysical Research: Atmospheres*, *122*(3), 2008–2025.

Figure 1.

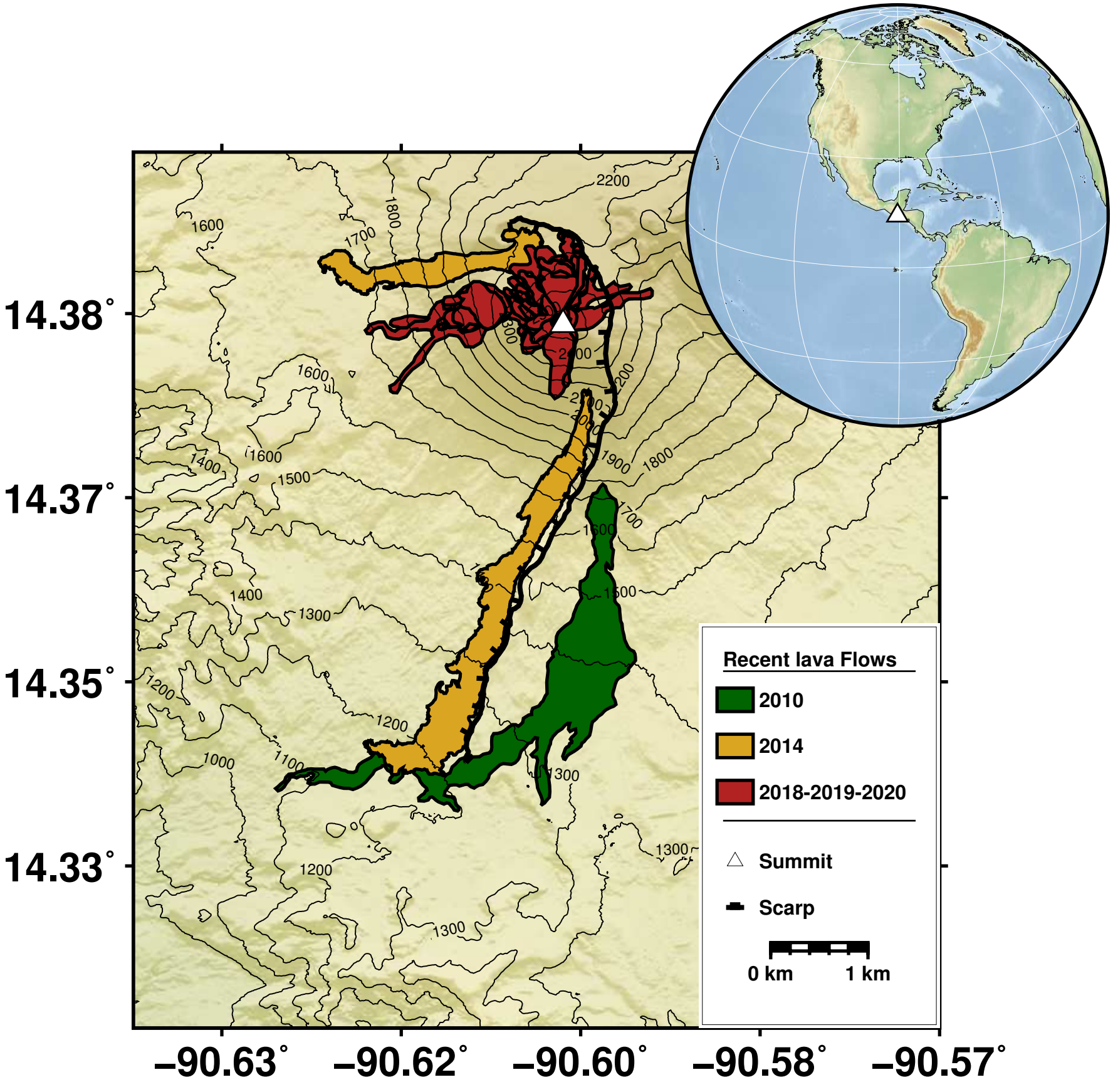
14.38˚
14.37˚
14.35˚
14.33˚
–90.63˚
–90.62˚
–90.60˚
–90.58˚
–90.57˚
Recent lava Flows
2010
2014
2018-2019-2020
Summit
Scarp
0 km
1 km

Figure 2.

a)

25/04/2015 - 14/01/2016

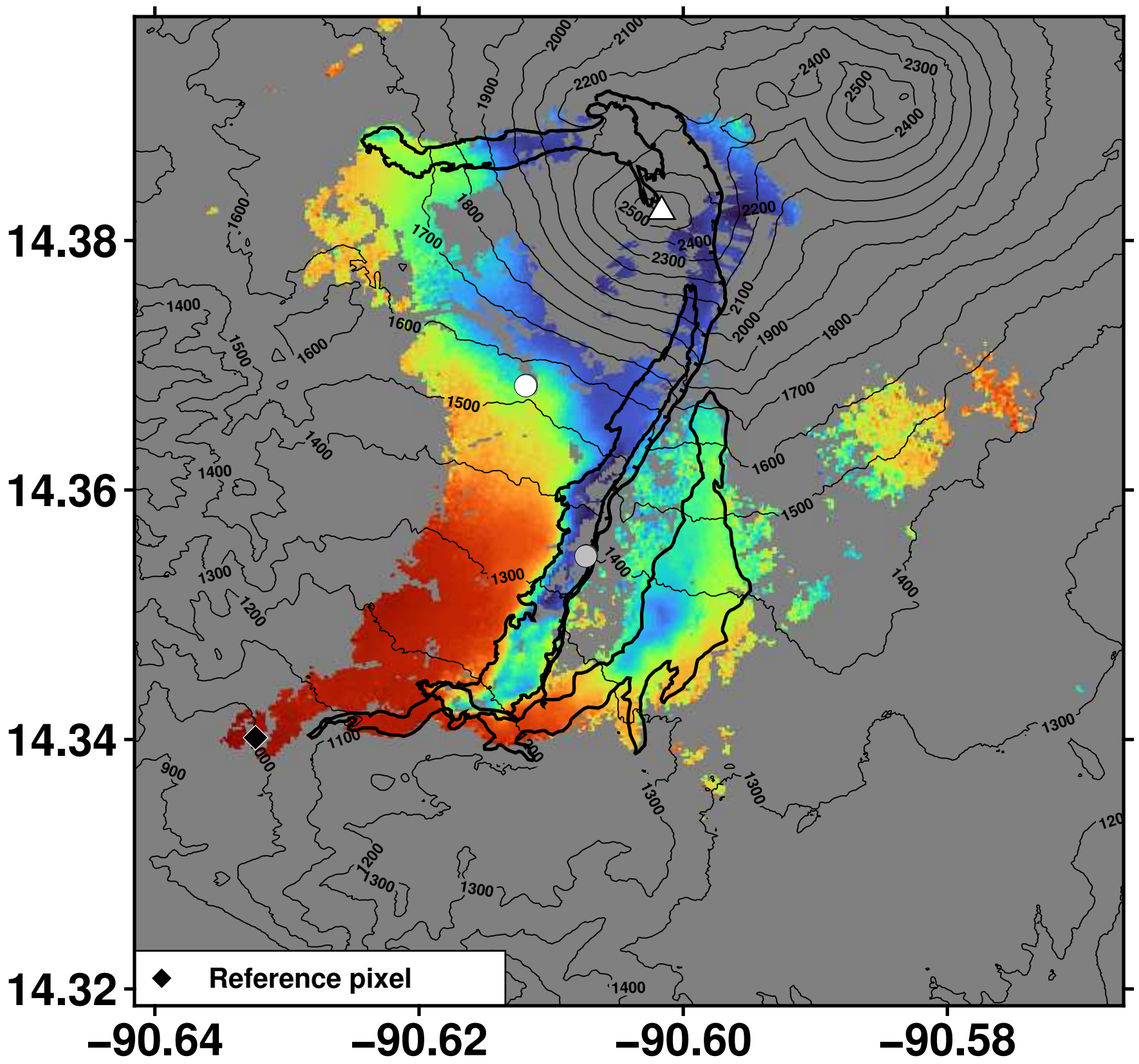

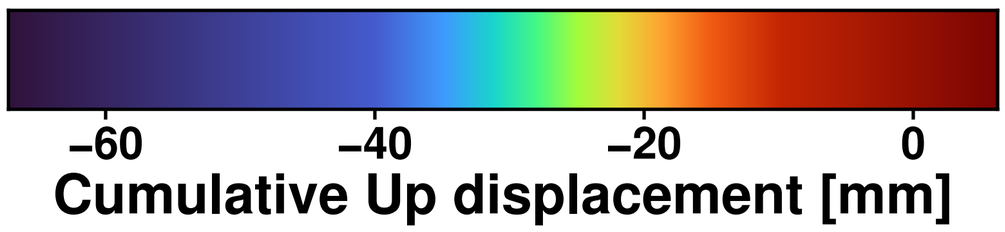

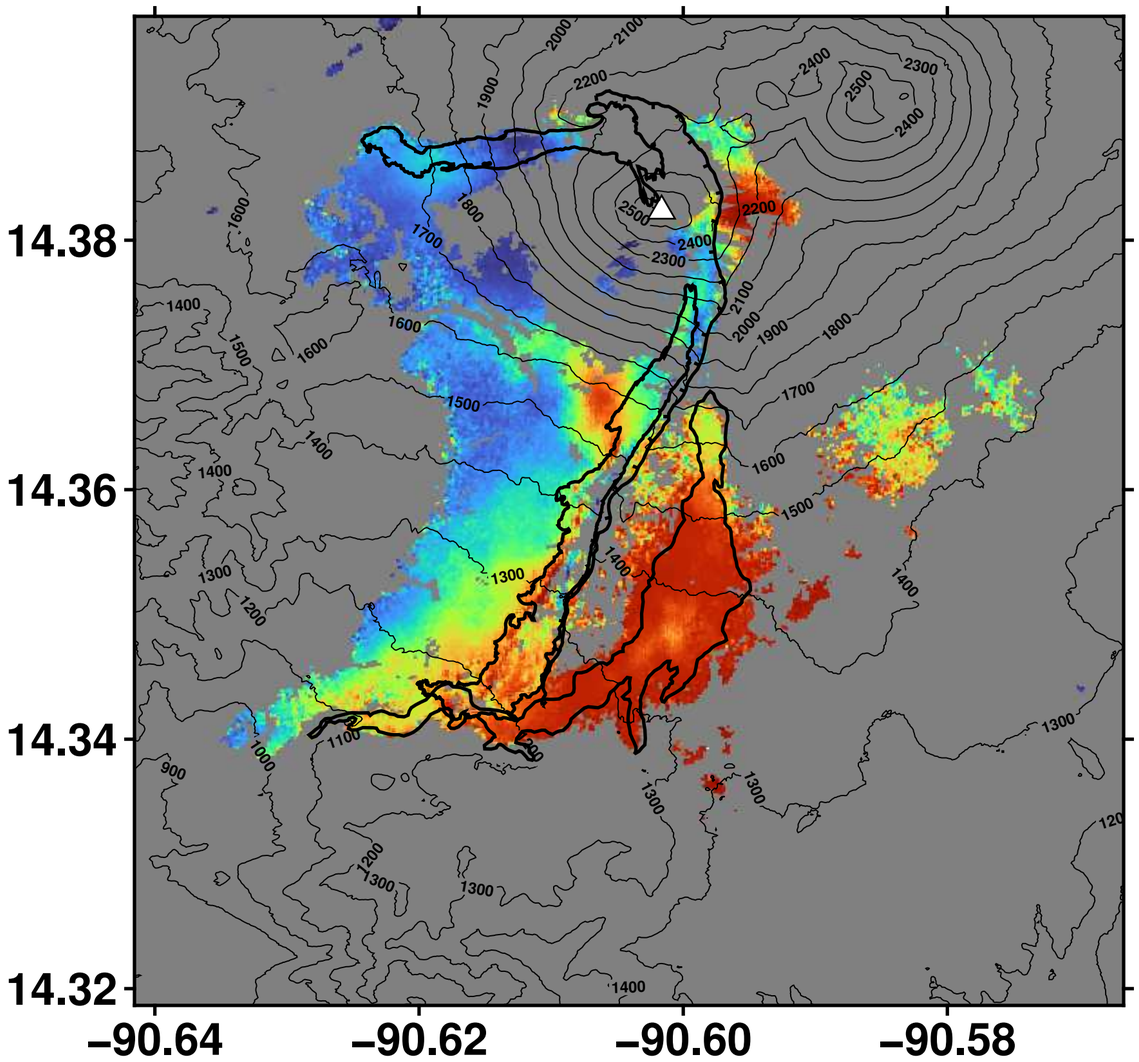

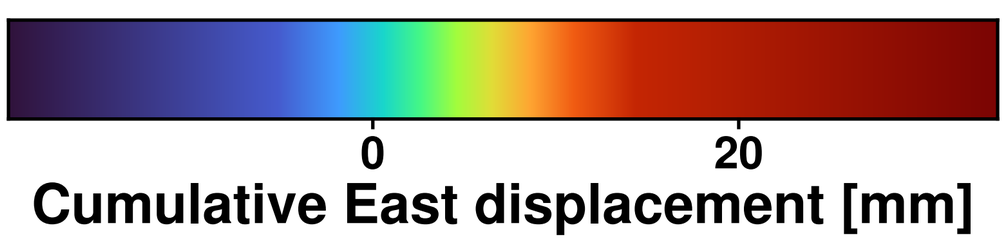

b)

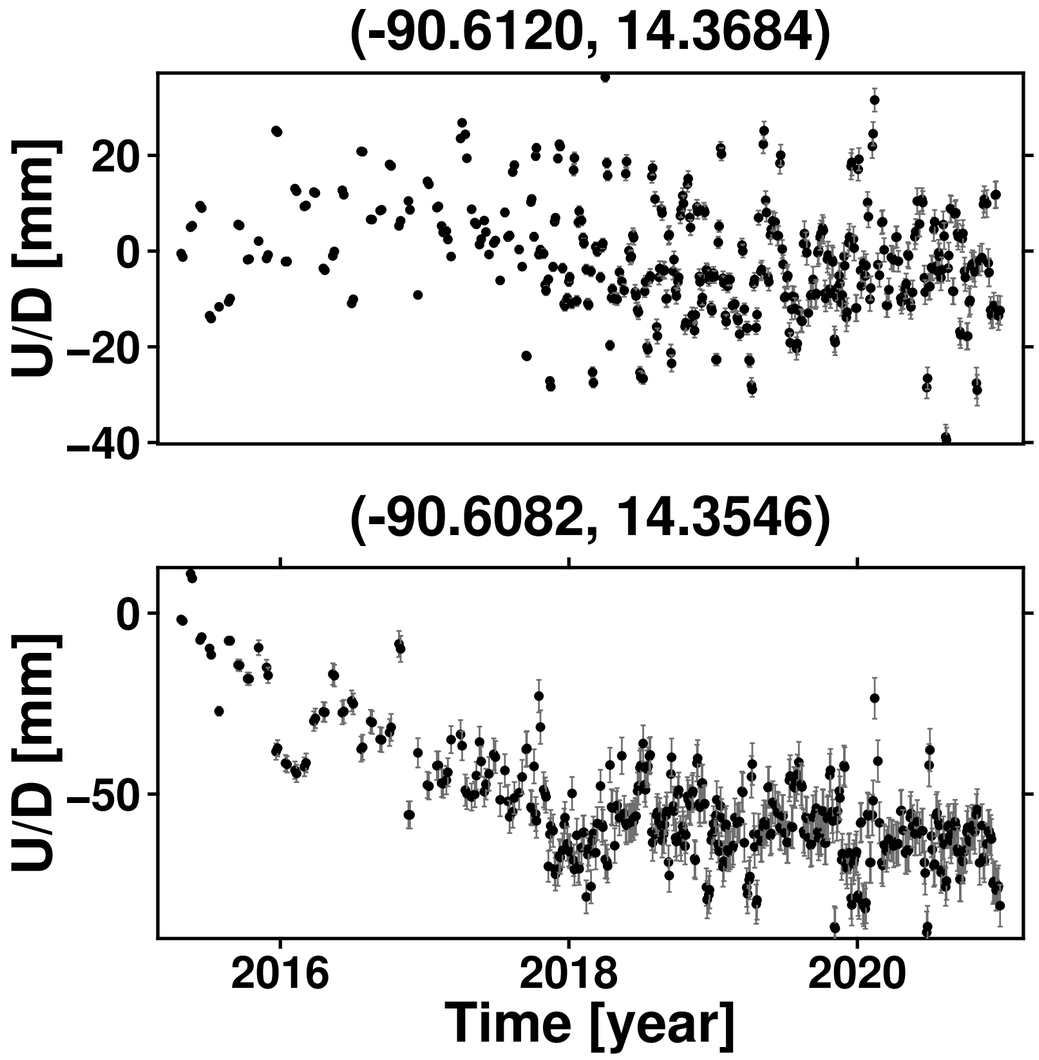

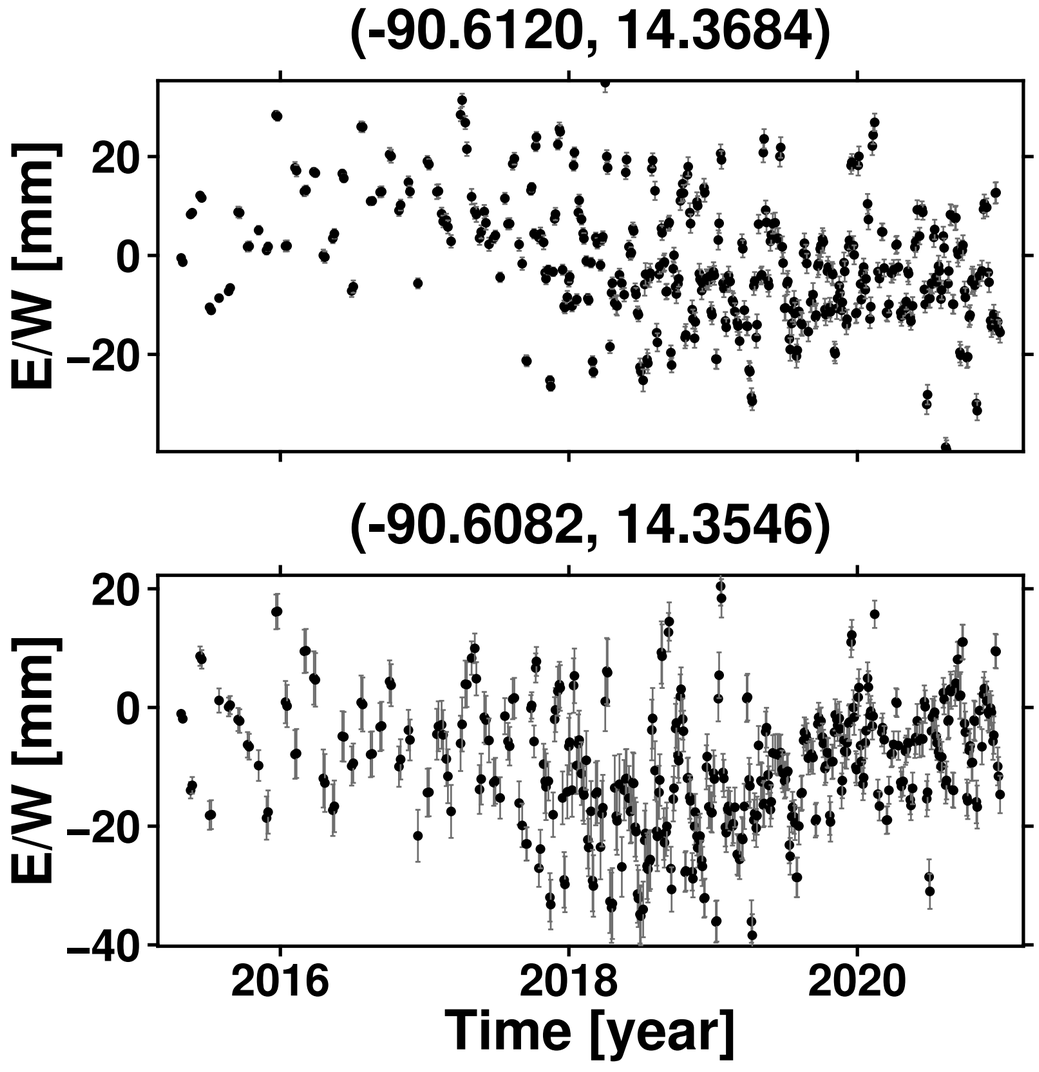

Figure 3.

a)

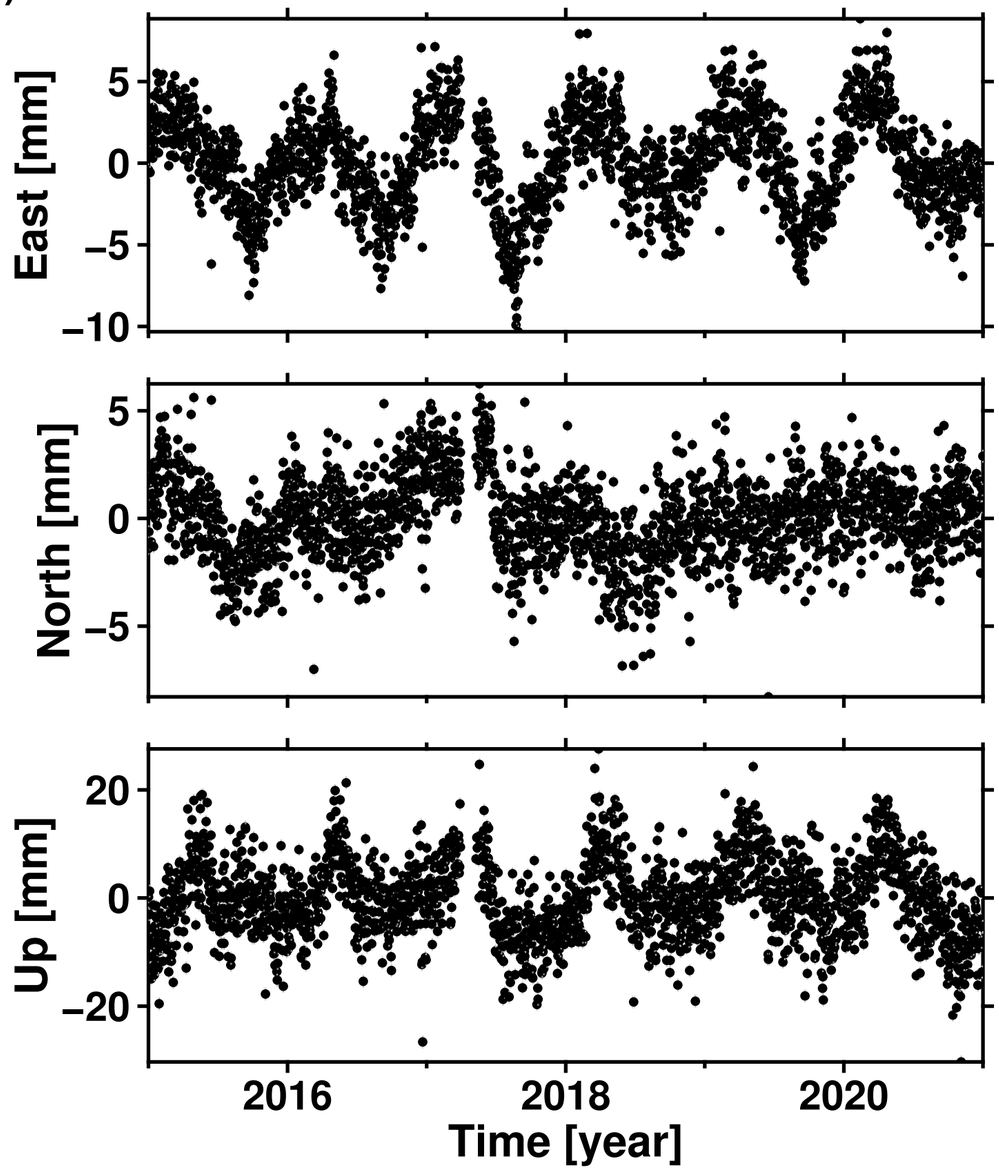
GPS (GUAT)
East [mm]
North [mm]
Up [mm]
5
0
−5
−10
20
−20
2016
2018
2020
Time [year]

b)

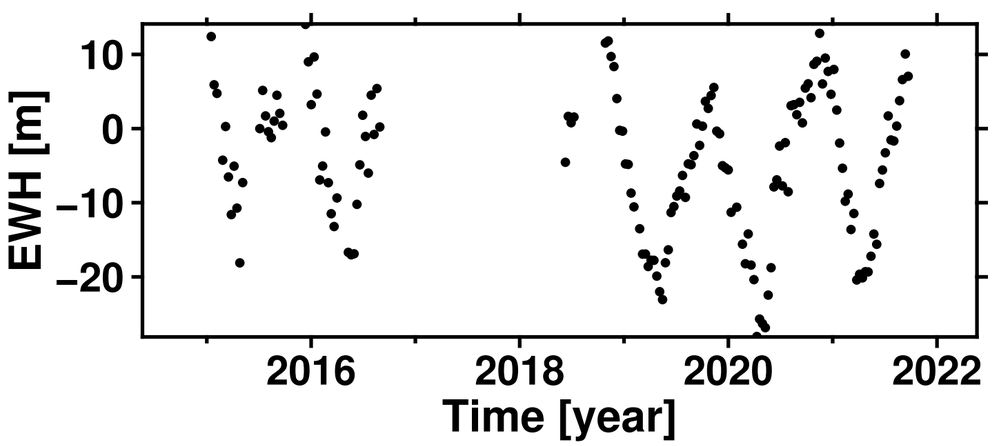
GRACE
EWH [m]
10
0
−10
−20
2016
2018
2020
2022
Time [year]

c)

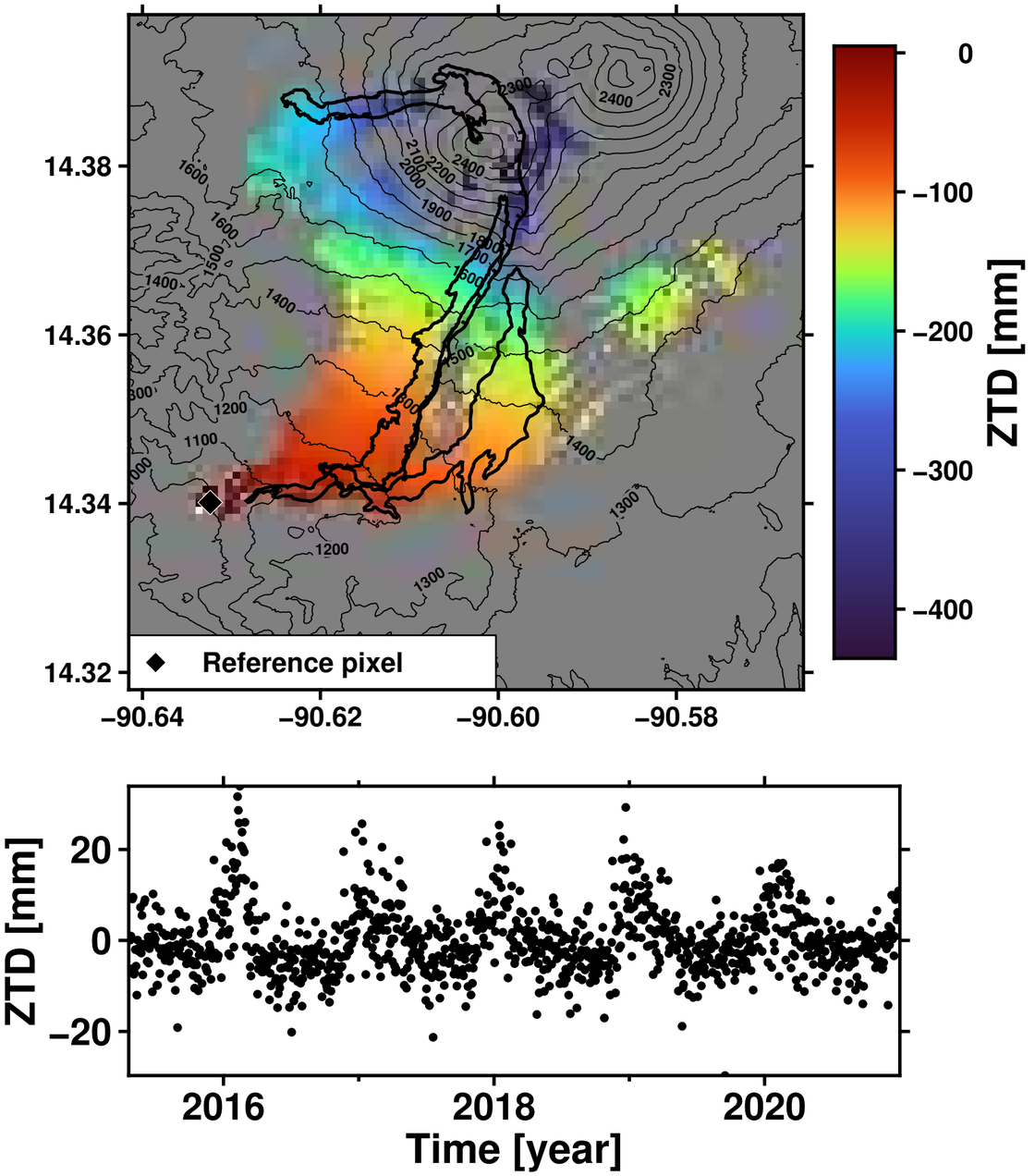
GACOS
14.38
14.36
14.34
14.32
−90.64
−90.62
−90.60
−90.58
Reference pixel
ZTD [mm]
0
−100
−200
−300
−400
ZTD [mm]
20
0
−20
2016
2018
2020
Time [year]

d)

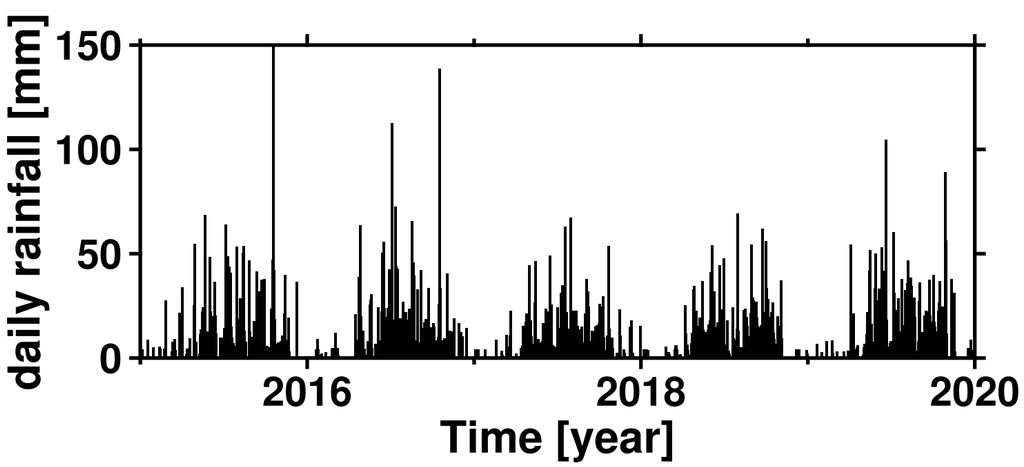
daily rainfall [mm]
150
100
50
0
2016
2018
2020
Time [year]

Figure 4.

a)

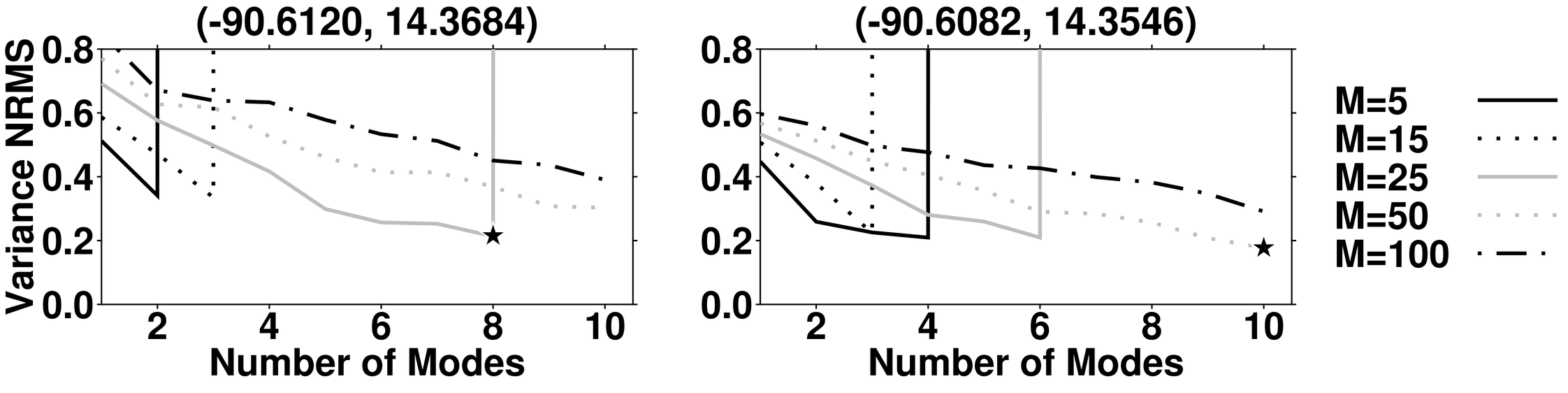
(-90.6120, 14.3684)
(-90.6082, 14.3546)
Variance NRMS
0.0
0.2
0.4
0.6
0.8
2
4
6
8
10
Number of Modes
M=5
M=15
M=25
M=50
M=100

b)

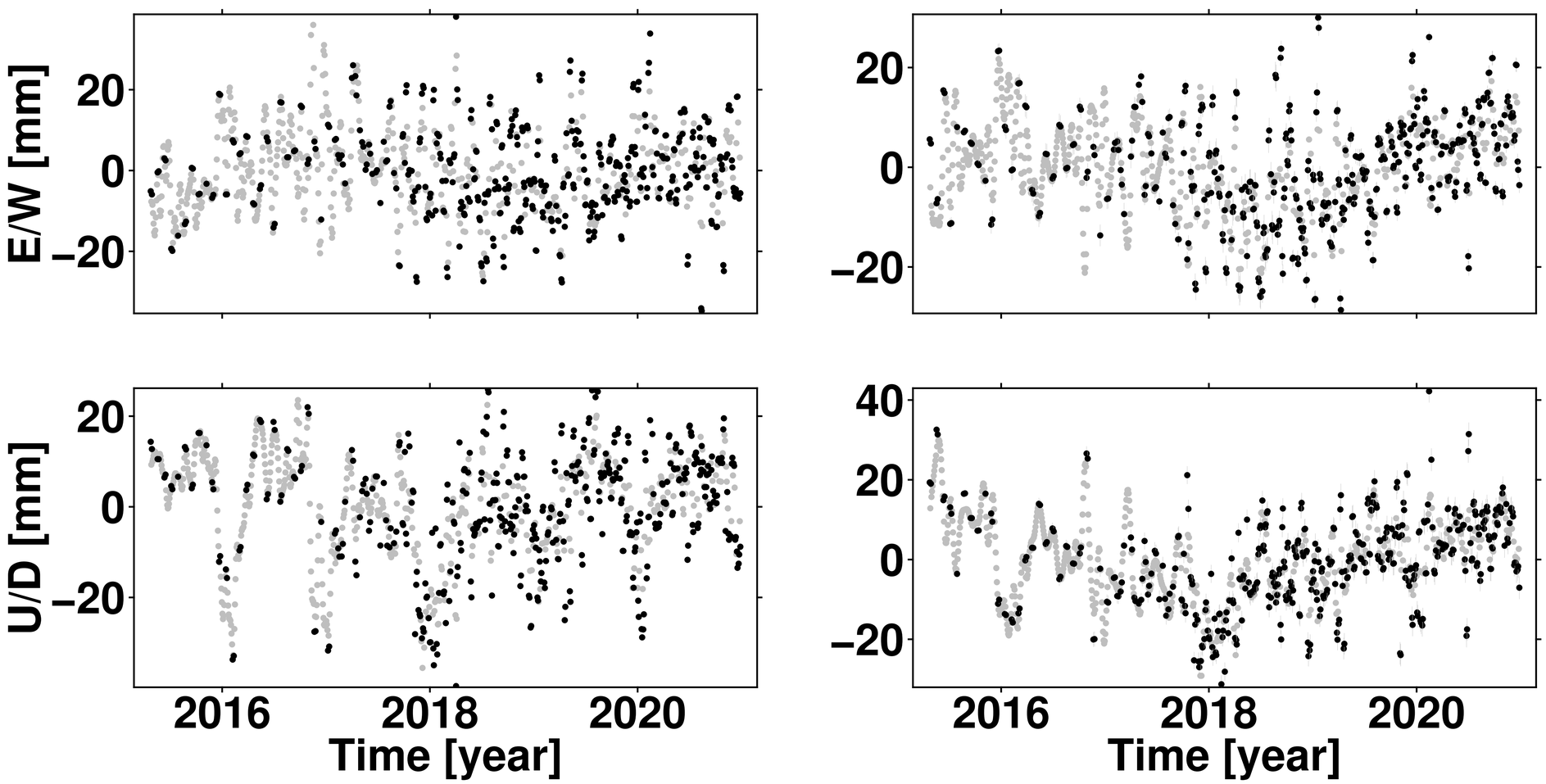
E/W [mm]
U/D [mm]
20
0
−20
40
2016
2018
2020
Time [year]

Figure 5.

a)

b)

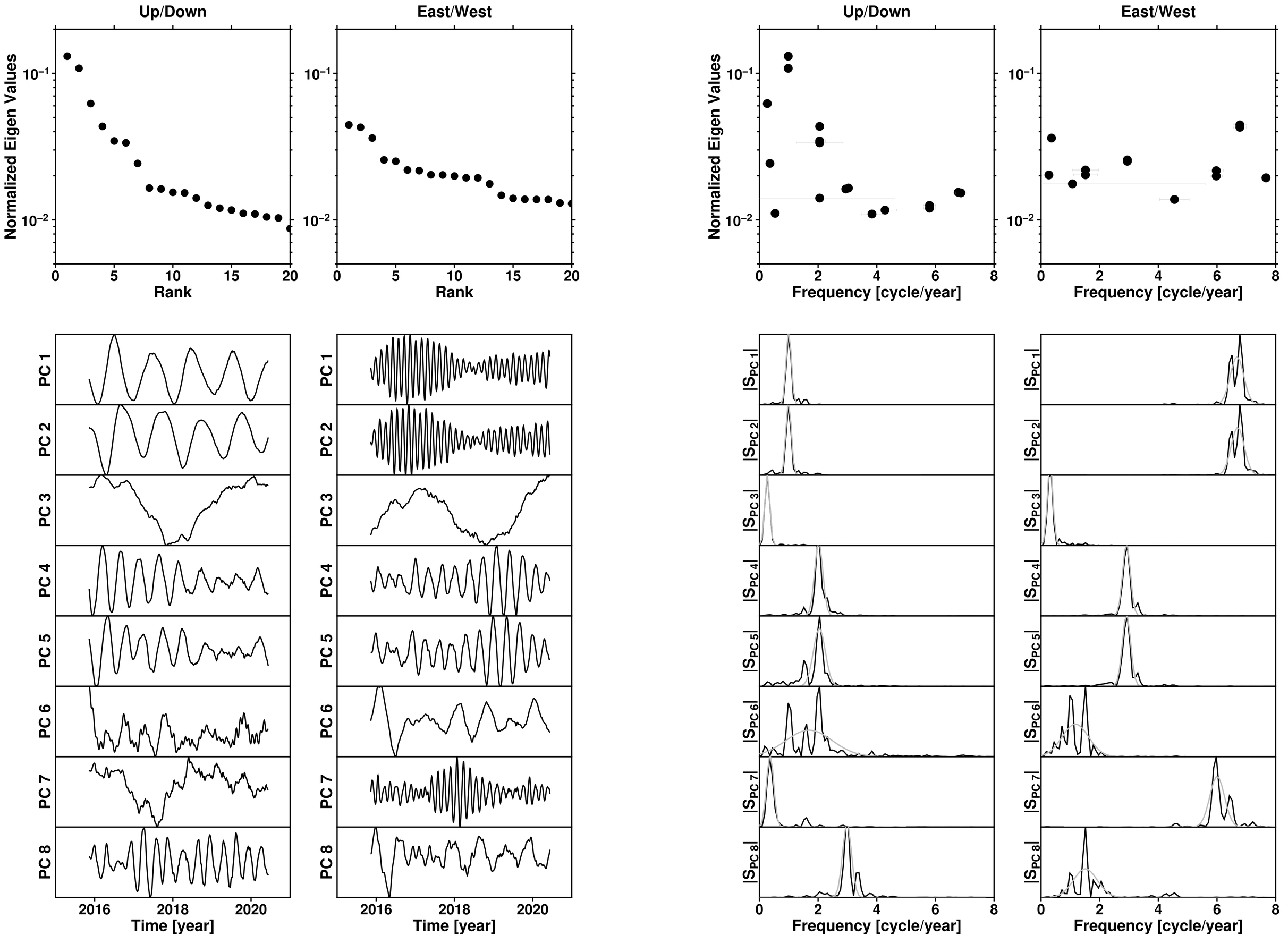
Up/Down
East/West
Normalized Eigen Values
10^{-1}
10^{-2}
Rank
Frequency [cycle/year]
PC 1
PC 2
PC 3
PC 4
PC 5
PC 6
PC 7
PC 8
$|S_{PC\,1}|$
$|S_{PC\,2}|$
$|S_{PC\,3}|$
$|S_{PC\,4}|$
$|S_{PC\,5}|$
$|S_{PC\,6}|$
$|S_{PC\,7}|$
$|S_{PC\,8}|$
2016
2018
2020
Time [year]

Figure 6.

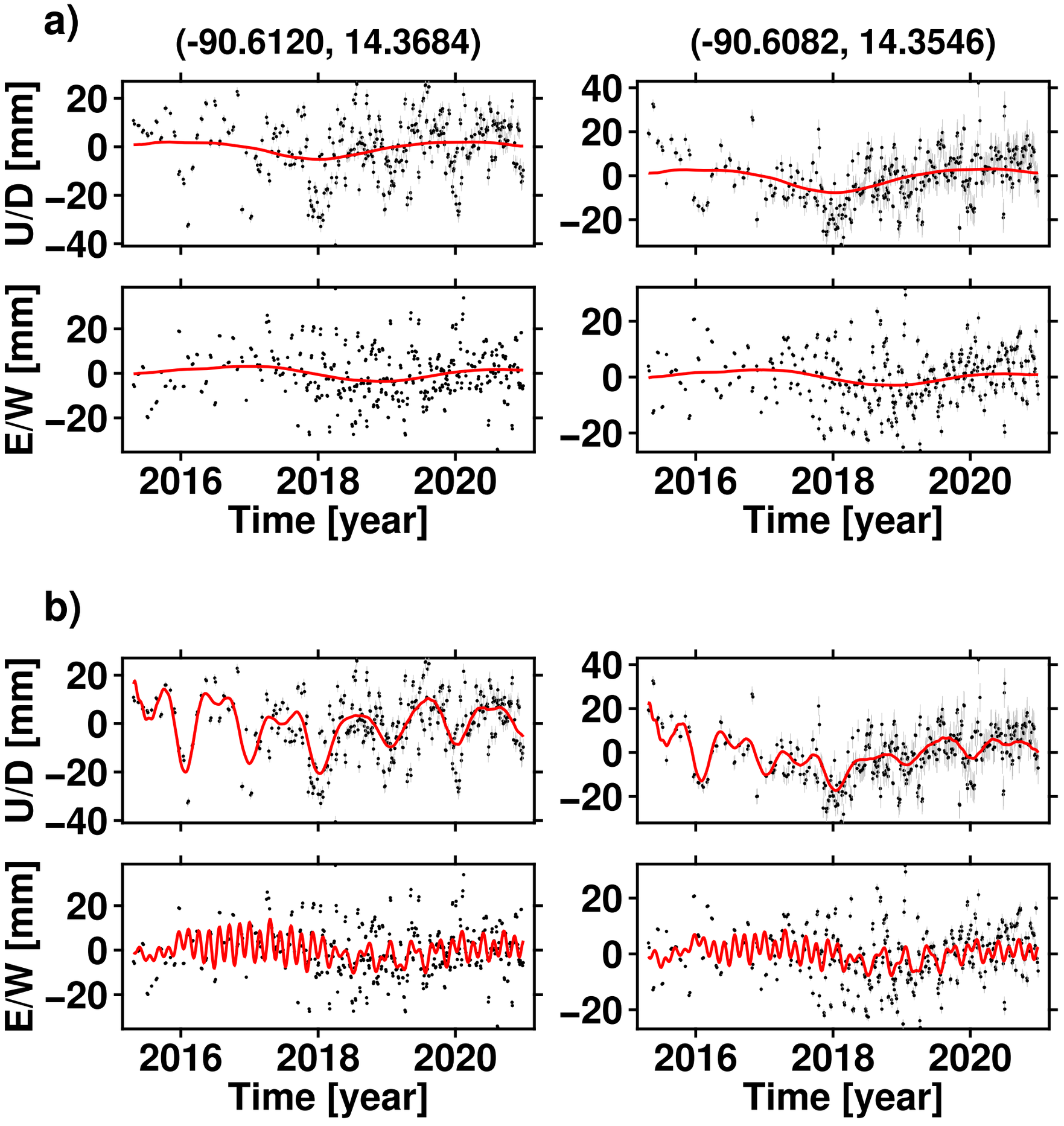
a)
(-90.6120, 14.3684)
(-90.6082, 14.3546)
U/D [mm]
E/W [mm]
20
0
−20
−40
40
2016
2018
2020
Time [year]
b)

Figure 7.

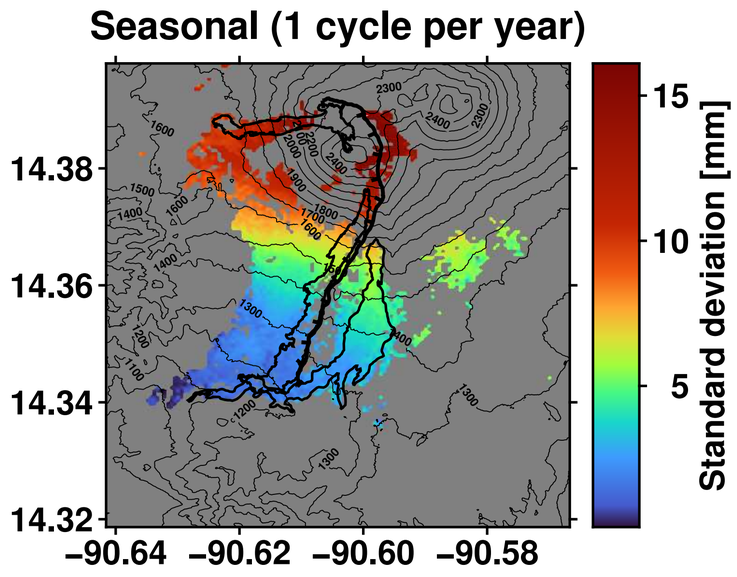
Seasonal (1 cycle per year)
14.38
14.36
14.34
14.32
−90.64
−90.62
−90.60
−90.58
15
10
5
Standard deviation [mm]

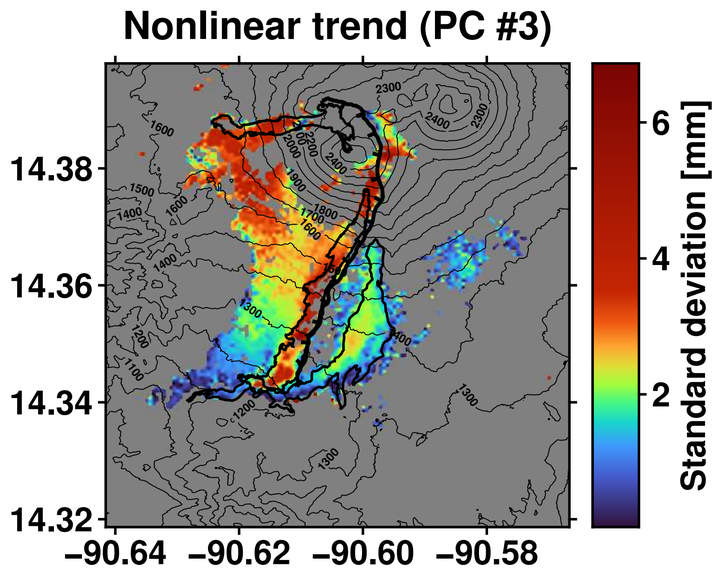
Nonlinear trend (PC #3)
14.38
14.36
14.34
14.32
−90.64
−90.62
−90.60
−90.58
6
4
2
Standard deviation [mm]

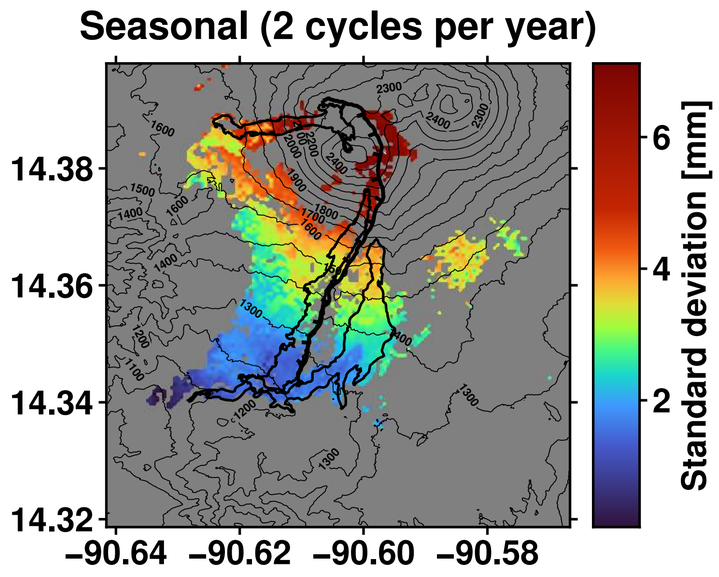
Seasonal (2 cycles per year)
14.38
14.36
14.34
14.32
−90.64
−90.62
−90.60
−90.58
6
4
2
Standard deviation [mm]

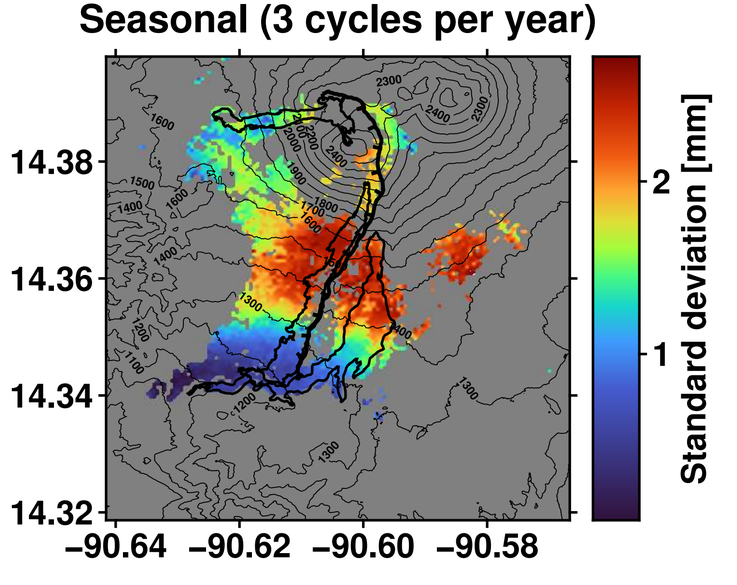
Seasonal (3 cycles per year)
14.38
14.36
14.34
14.32
−90.64
−90.62
−90.60
−90.58
2
1
Standard deviation [mm]

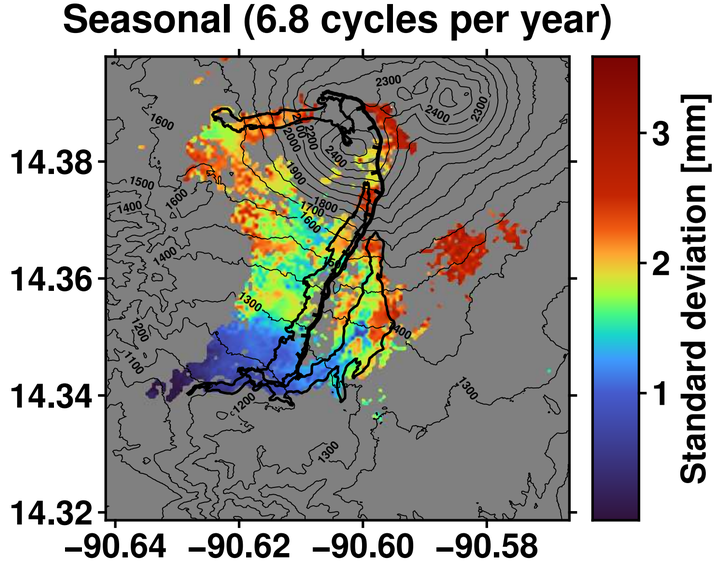
Seasonal (6.8 cycles per year)
14.38
14.36
14.34
14.32
−90.64
−90.62
−90.60
−90.58
3
2
1
Standard deviation [mm]

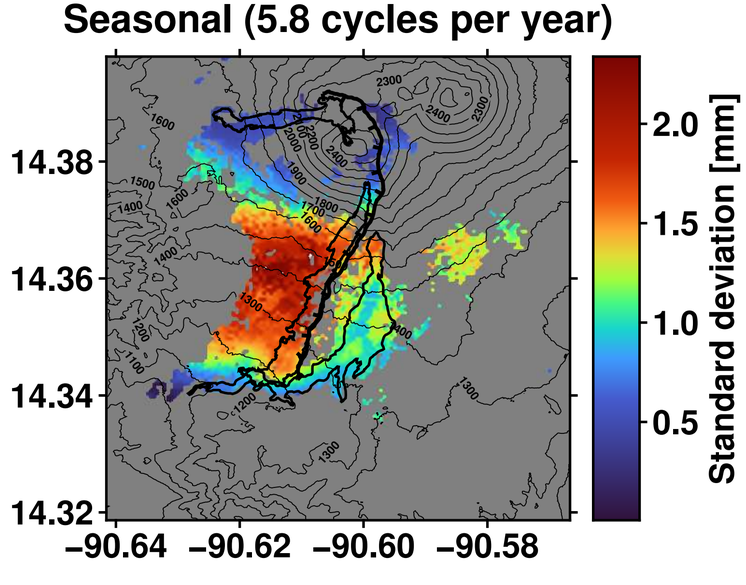
Seasonal (5.8 cycles per year)
14.38
14.36
14.34
14.32
−90.64
−90.62
−90.60
−90.58
2.0
1.5
1.0
0.5
Standard deviation [mm]

Figure 8.

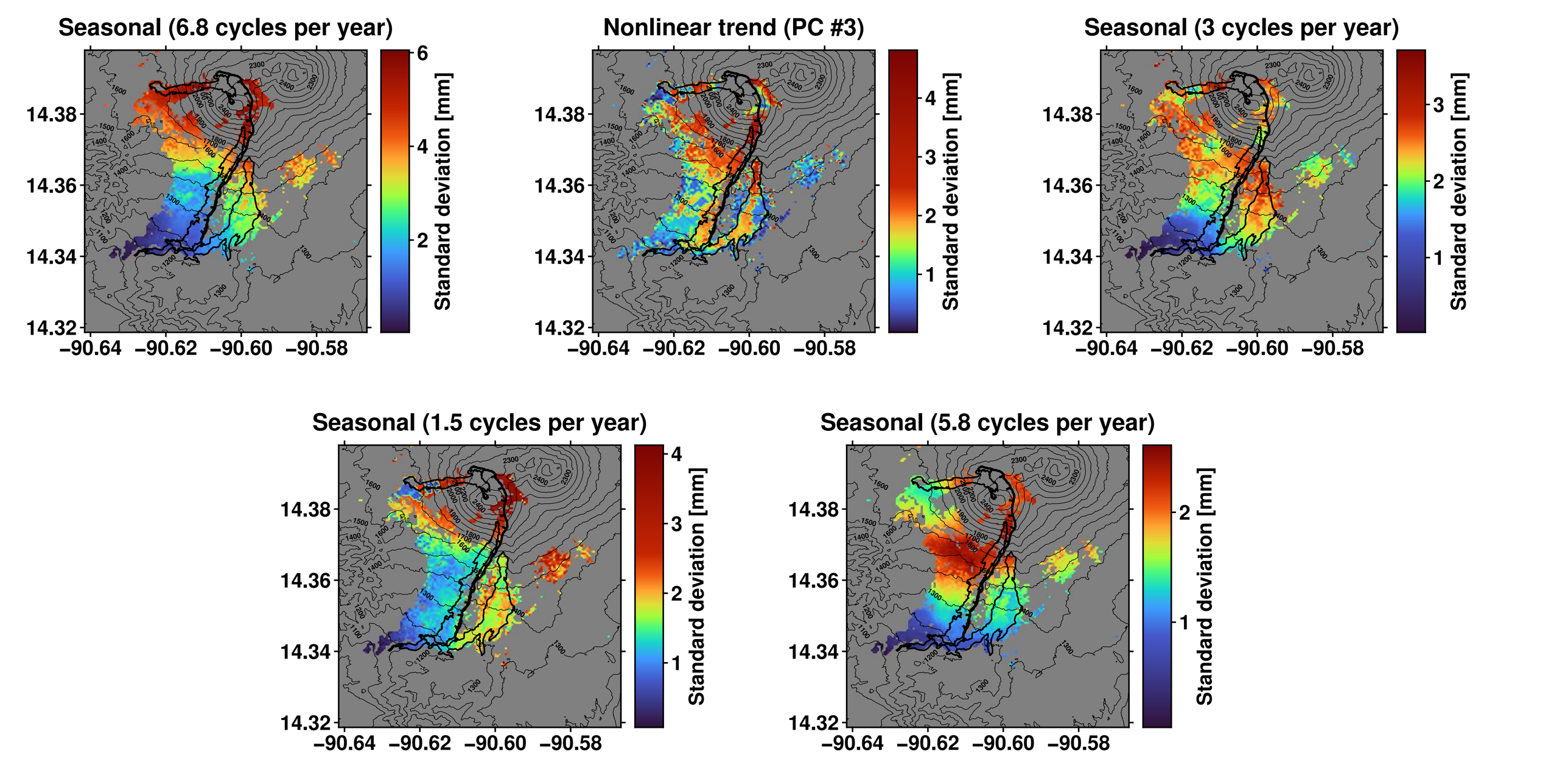
Seasonal (6.8 cycles per year)
Nonlinear trend (PC #3)
Seasonal (3 cycles per year)
Seasonal (1.5 cycles per year)
Seasonal (5.8 cycles per year)
Standard deviation [mm]
14.38
14.36
14.34
14.32
−90.64
−90.62
−90.60
−90.58

Figure 9.

a)

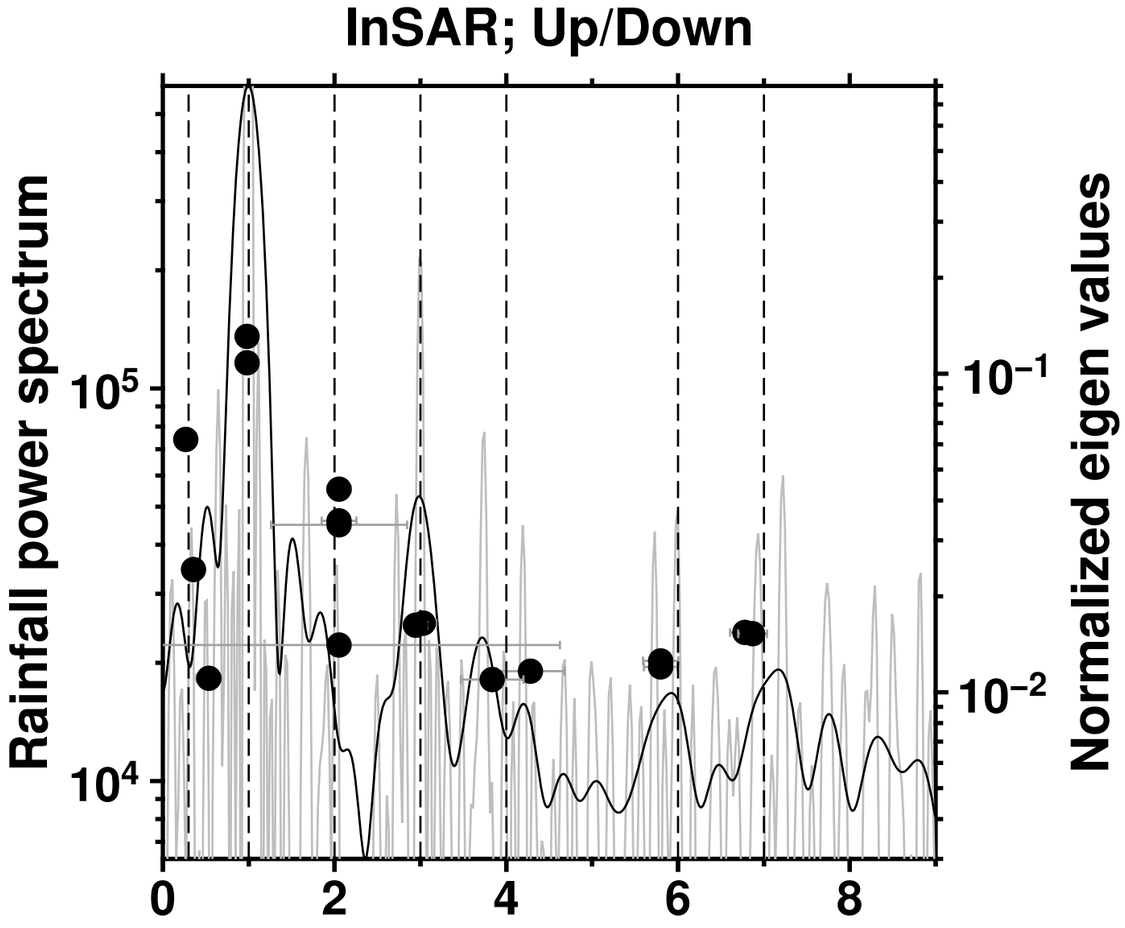
InSAR; Up/Down
Rainfall power spectrum
Normalized eigen values
10^5
10^4
10^{-1}
10^{-2}
0
2
4
6
8

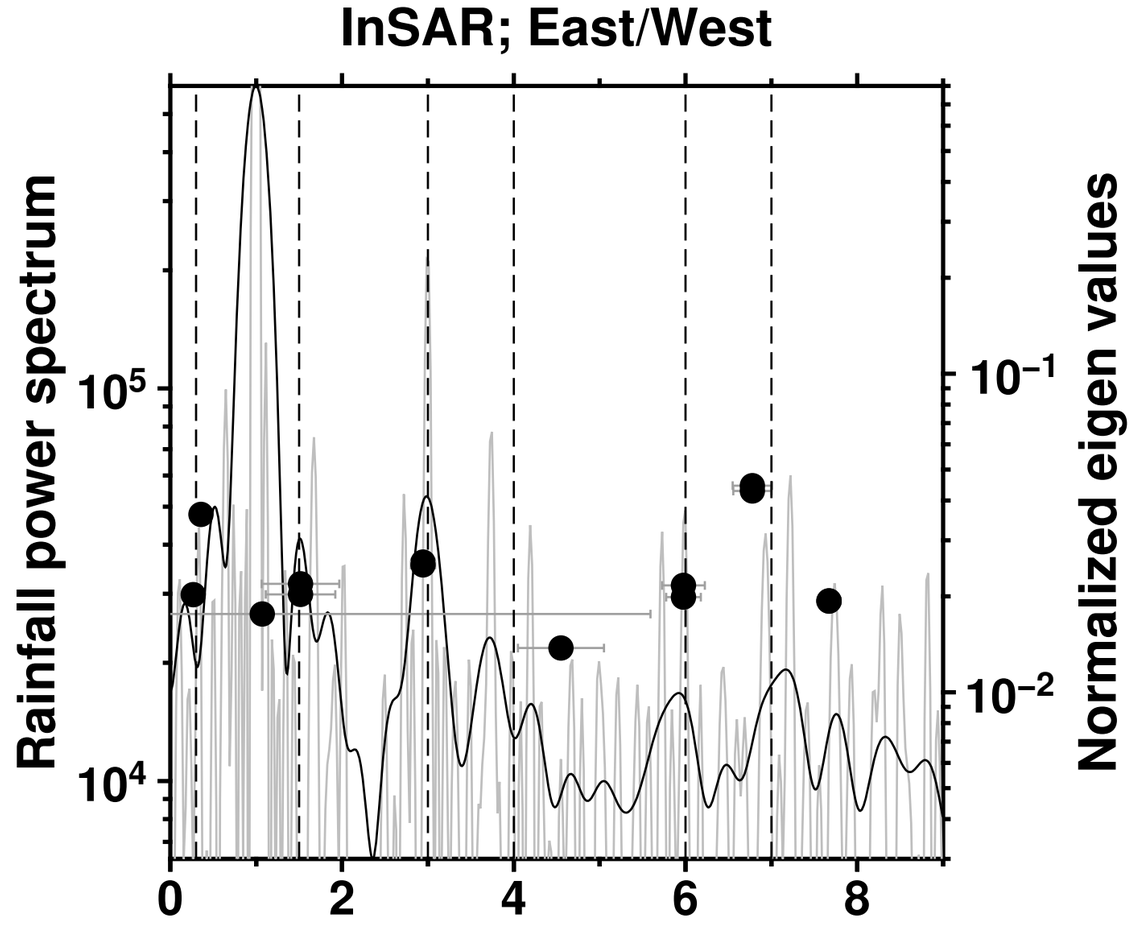
InSAR; East/West
Rainfall power spectrum
Normalized eigen values
10^5
10^4
10^{-1}
10^{-2}
0
2
4
6
8

b)

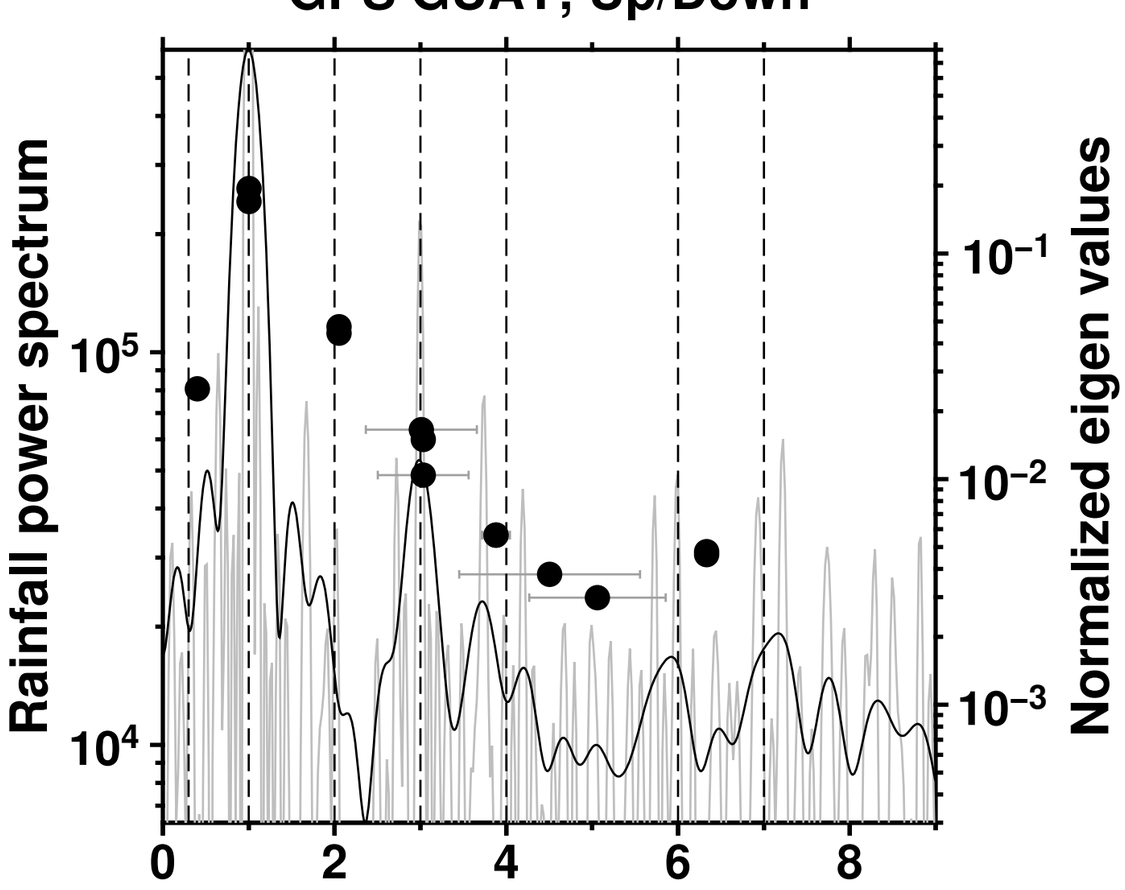
GPS GUAT; Up/Down
Rainfall power spectrum
Normalized eigen values
10^5
10^4
10^{-1}
10^{-2}
10^{-3}
0
2
4
6
8

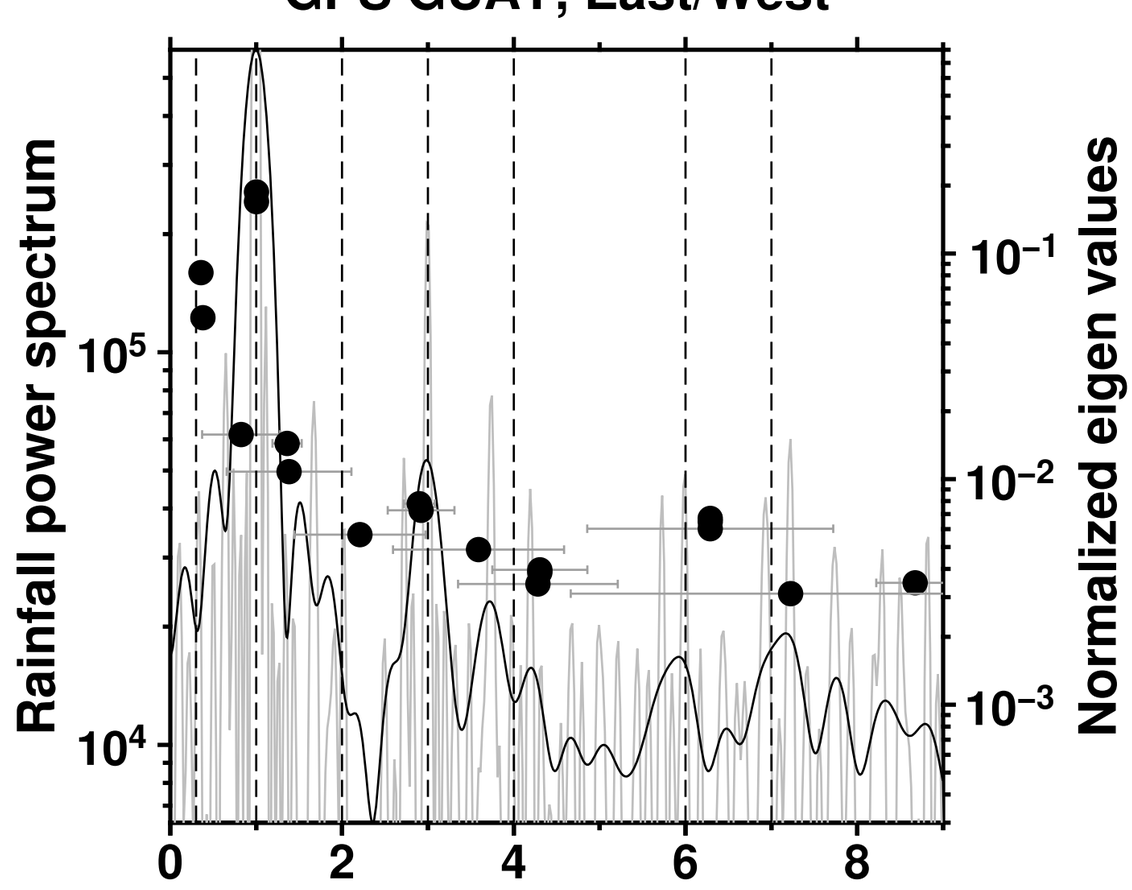
GPS GUAT; East/West
Rainfall power spectrum
Normalized eigen values
10^5
10^4
10^{-1}
10^{-2}
10^{-3}
0
2
4
6
8

c)

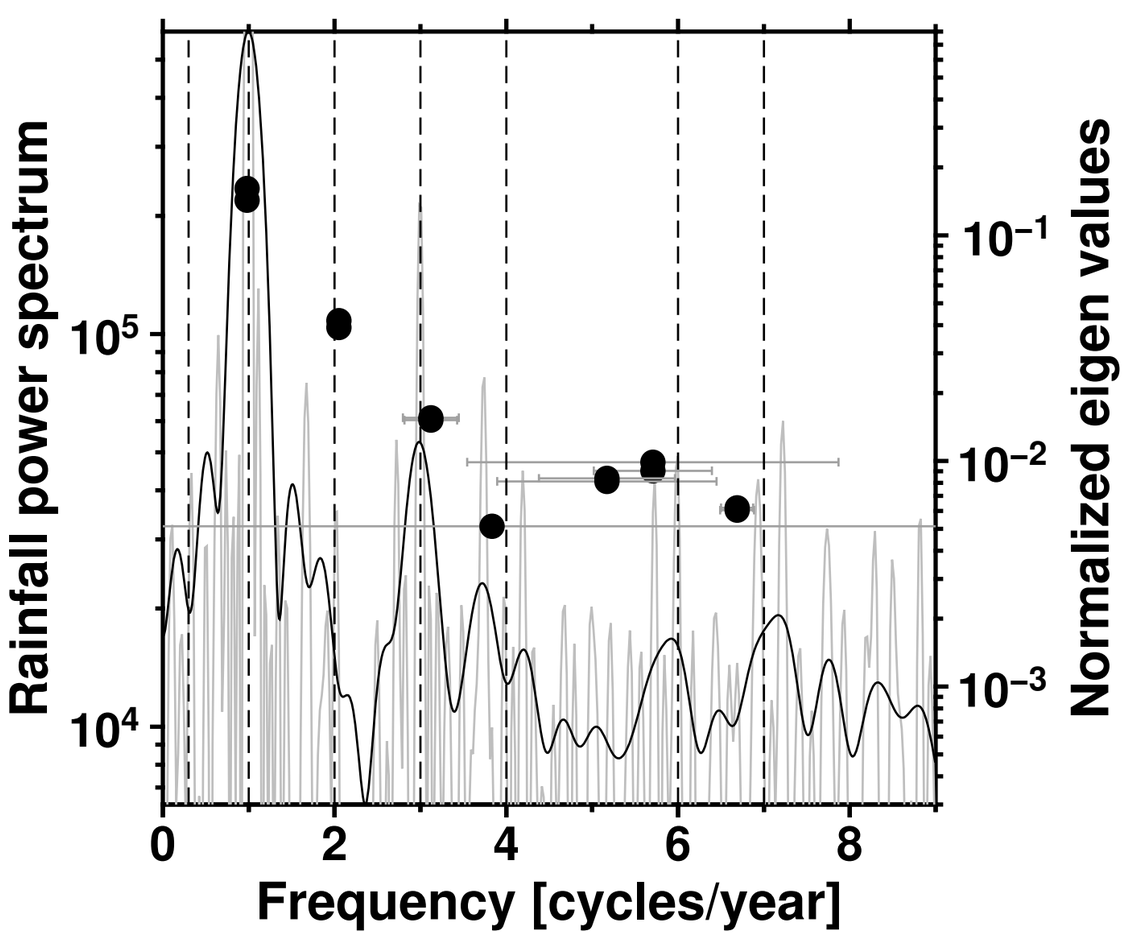
GACOS
Rainfall power spectrum
Normalized eigen values
10^5
10^4
10^{-1}
10^{-2}
10^{-3}
0
2
4
6
8
Frequency [cycles/year]

d)

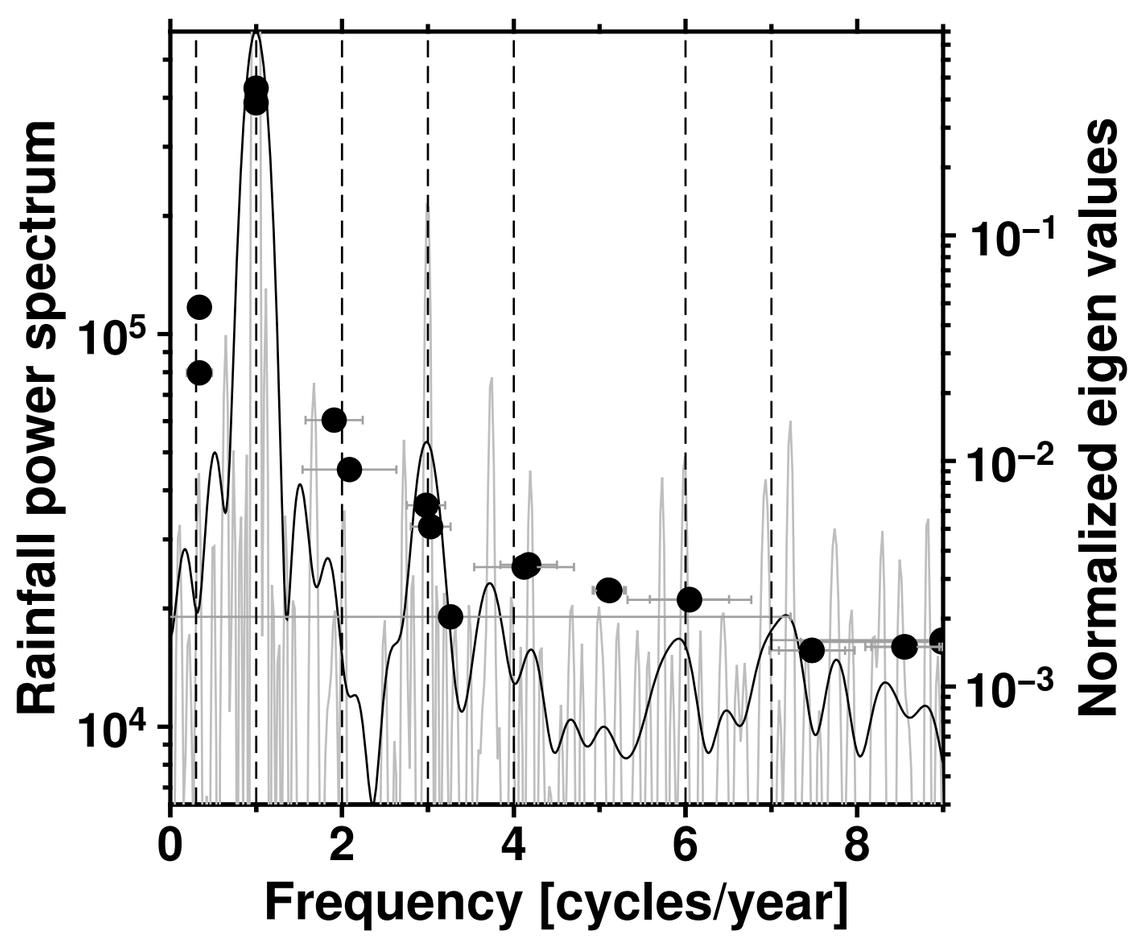
GRACE
Rainfall power spectrum
Normalized eigen values
10^5
10^4
10^{-1}
10^{-2}
10^{-3}
0
2
4
6
8
Frequency [cycles/year]

Figure 10.

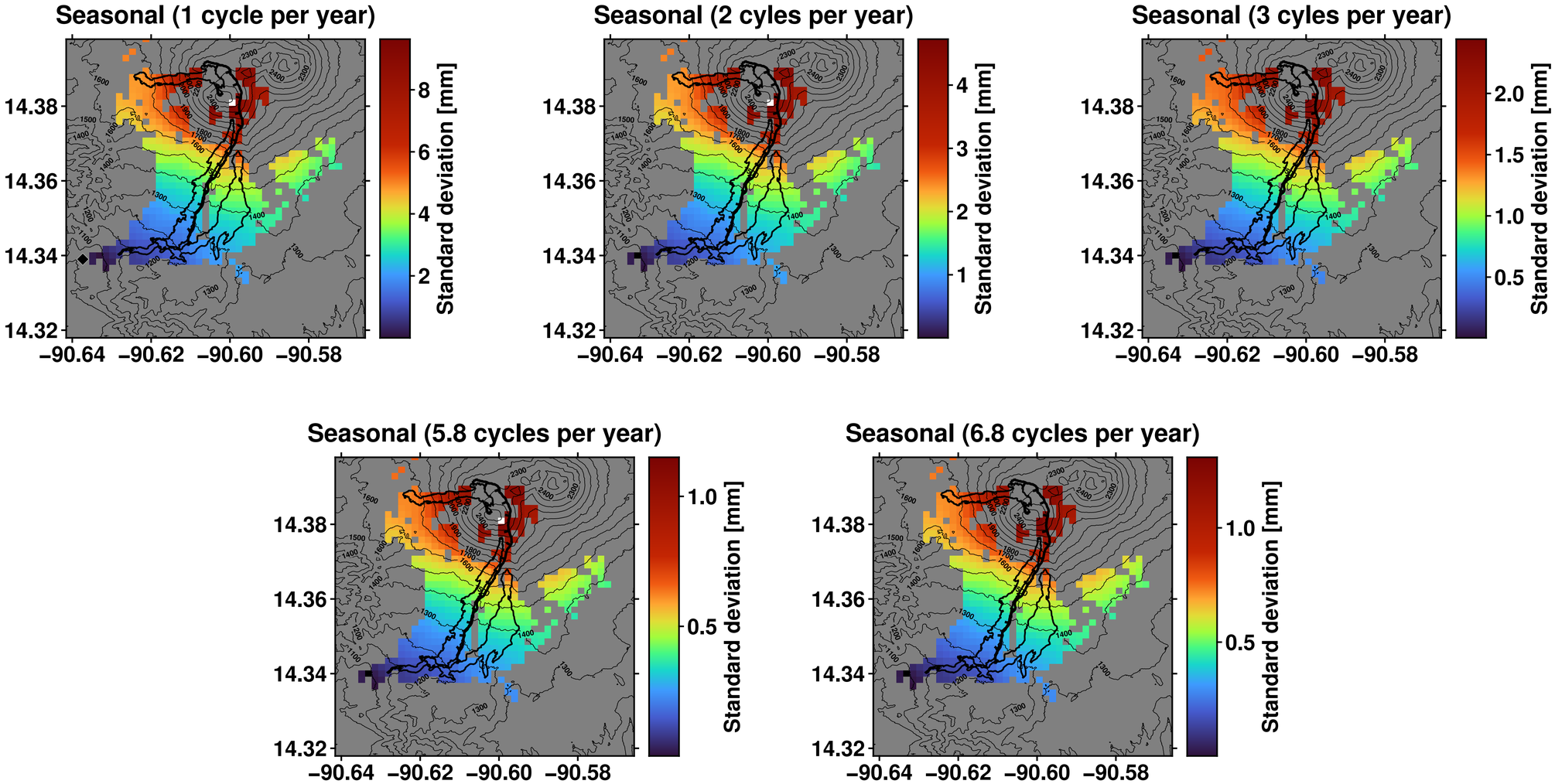
Seasonal (1 cycle per year)
Seasonal (2 cyles per year)
Seasonal (3 cyles per year)
Seasonal (5.8 cycles per year)
Seasonal (6.8 cycles per year)
Standard deviation [mm]
14.38
14.36
14.34
14.32
−90.64
−90.62
−90.60
−90.58

Figure 11.

a)

Sentinel 1 (Up/Down)

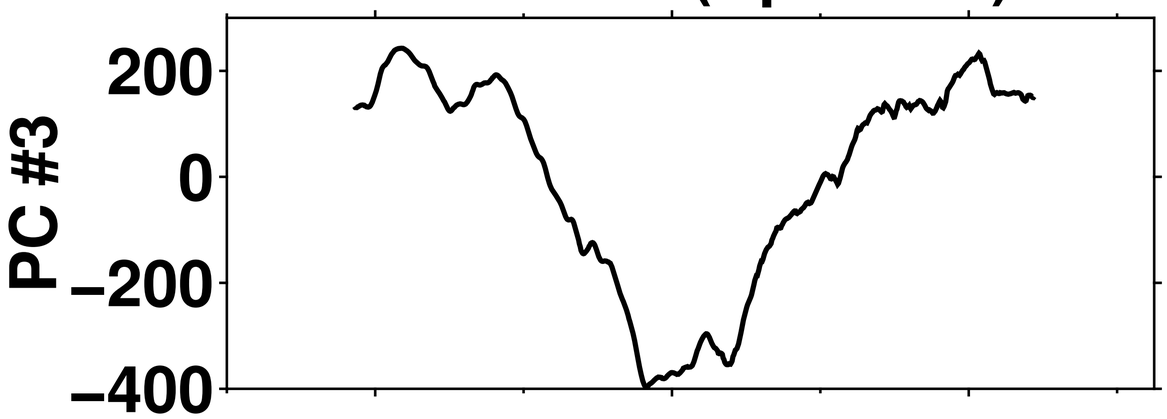

Sentinel 1 (East/West)

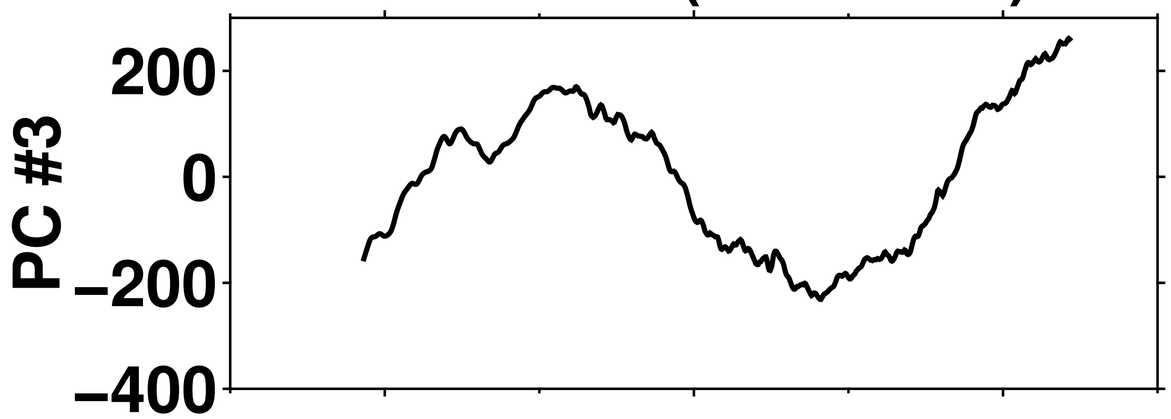

b)

GPS GUAT (Up/Down)

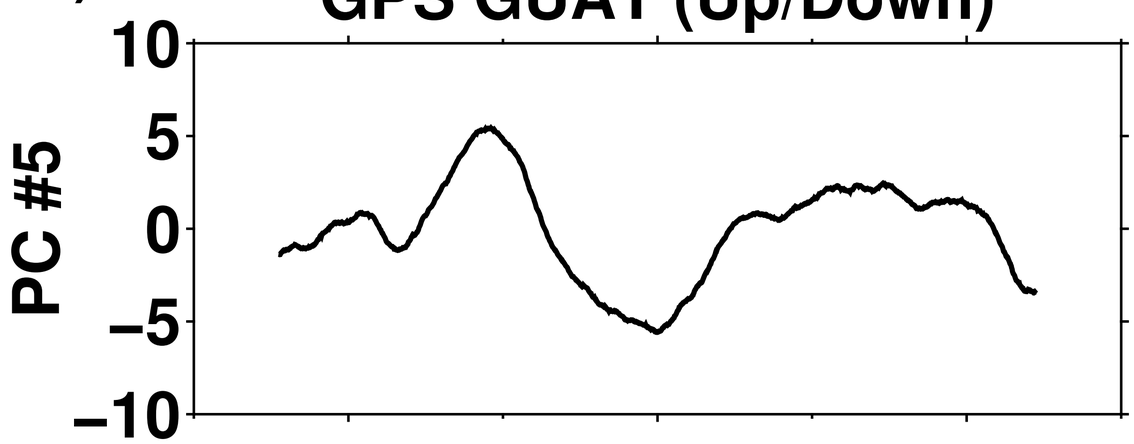

GPS GUAT (Horizontal)

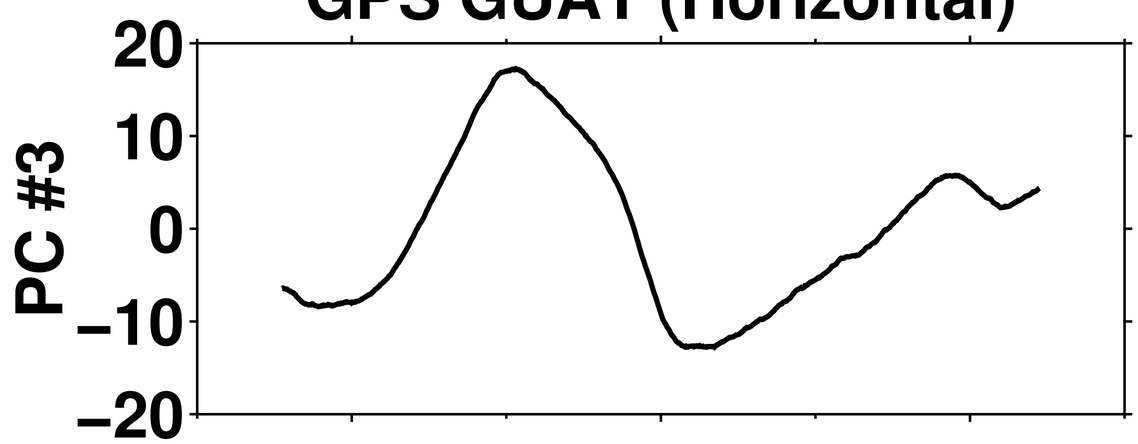

c)

Daily rainfall moving average

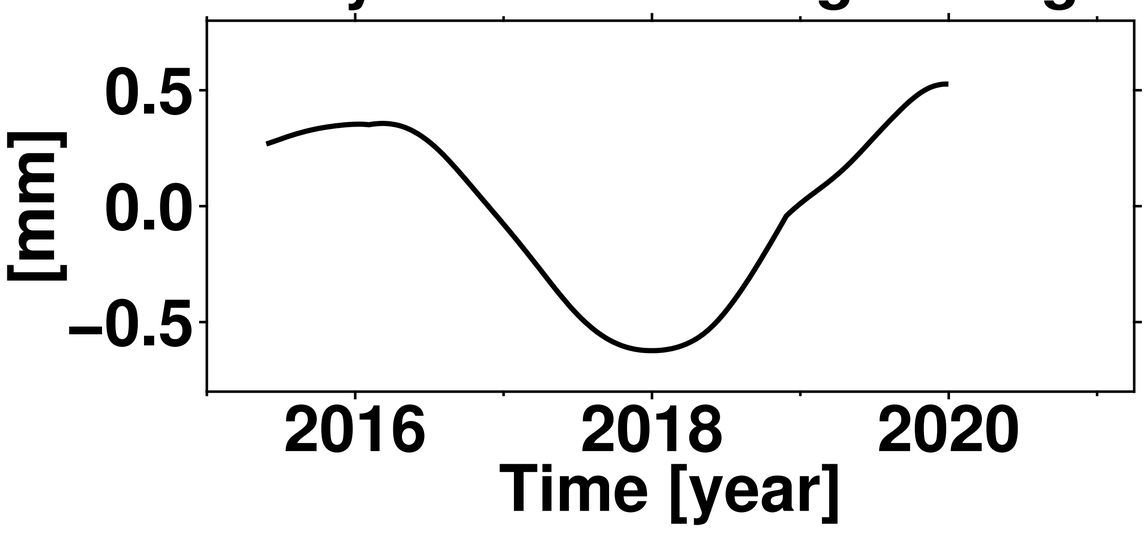

Detrended cumulative rainfall

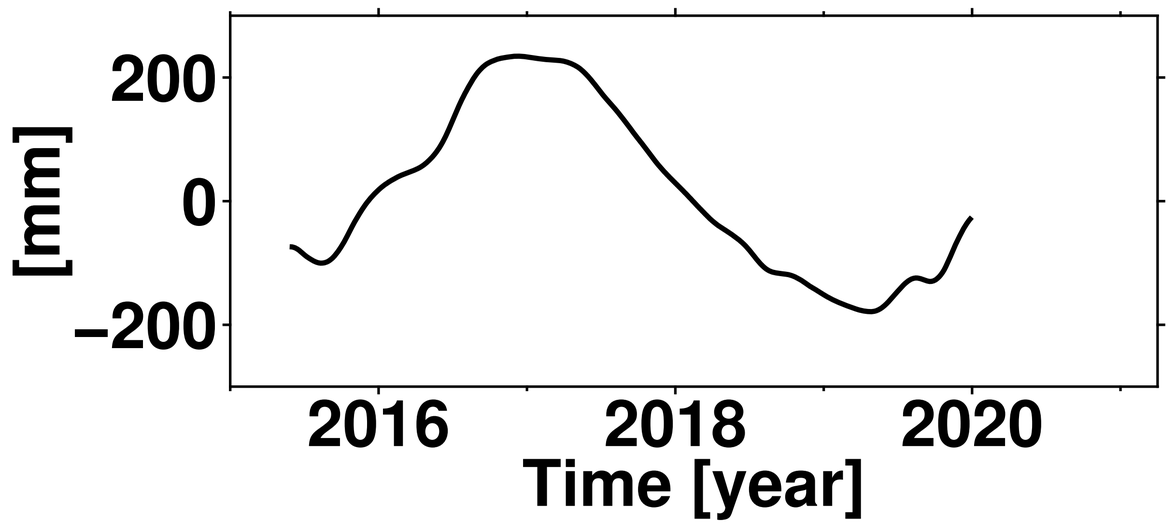

d)

GRACE